

Fast Lightcones for Combined Cosmological Probes

Raphaël Sgier,^{1,a} Janis Fluri,^a Jörg Herbel,^a Alexandre Réfrégier,^a Adam Amara,^{a,b} Tomasz Kacprzak,^a Andrina Nicola^c

^aInstitute for Particle Physics and Astrophysics, Department of Physics, ETH Zurich, Wolfgang-Pauli-Strasse 27, 8093 Zurich, Switzerland

^bInstitute of Cosmology & Gravitation, University of Portsmouth, Dennis Sciamia Building, Burnaby Road, Portsmouth PO1 3FX, UK

^cDepartment of Astrophysical Sciences, Princeton University, Peyton Hall, Princeton NJ08544-0010, USA

Abstract. The combination of different cosmological probes offers stringent tests of the Λ CDM model and enhanced control of systematics. For this purpose, we present an extension of the lightcone generator UFALCON first introduced in Sgier *et al.* [1], enabling the simulation of a self-consistent set of maps for different cosmological probes. Each realization is generated from the same underlying simulated density field, and contains full-sky maps of different probes, namely weak lensing shear, galaxy overdensity including RSD, CMB lensing, and CMB temperature anisotropies from the ISW effect. The lightcone generation performed by UFALCON is parallelized and based on the replication of a large periodic volume simulated with the GPU-accelerated N -Body code PKDGRAV3. The post-processing to construct the lightcones requires only a runtime of about 1 walltime-hour corresponding to about 100 CPU-hours. We use a randomization procedure to increase the number of quasi-independent full-sky UFALCON map-realizations, which enables us to compute an accurate multi-probe covariance matrix. Using this framework, we forecast cosmological parameter constraints by performing a multi-probe likelihood analysis for a combination of simulated future stage-IV-like surveys. We find that the inclusion of the cross-correlations between the probes significantly increases the information gain in the parameter constraints. We also find that the use of a non-Gaussian covariance matrix is increasingly important, as more probes and cross-correlation power spectra are included. A version of the UFALCON package currently including weak gravitational lensing is publicly available.²

¹Corresponding author, Email: raphael.sgier@phys.ethz.ch

²UFALCON: <https://cosmology.ethz.ch/research/software-lab/UFalcon.html>

Contents

1	Introduction	1
2	Analytical Predictions	5
3	Numerical Methods	8
3.1	N-Body Simulation	8
3.2	Lightcone Construction	9
3.2.1	Projected Lightcone	10
3.2.2	Interpolated Lightcone	13
3.3	Systematic Effects	14
3.3.1	Simulation Resolution	14
3.3.2	Super-Sample Covariance Effects	15
3.3.3	Shot Noise Estimation	15
3.3.4	Shell Randomization Procedure	16
3.3.5	Further Effects	17
3.4	Codebase	18
4	Statistical Analysis	18
4.1	1-Point Distribution	19
4.2	Spherical Harmonic Power Spectrum	20
4.3	Multi-Probe Covariance Matrix	20
5	Forecast	23
6	Conclusion	29
A	Analytical Prediction for the ISW Auto-Correlation	38
B	Shot Noise Estimation	40
C	Correlated Gaussian Maps	41
D	Pseudo-C_ℓ Estimation	42
E	CMB Lensing	45
F	Parameter Constraints with Nuisance Parameters	47

1 Introduction

The beginning of the era of precision cosmology has lead to the establishment of the Λ CDM model for cosmology. In spite of this remarkable success, the nature of dark energy and dark matter (DM) is still poorly understood and remains one of the greatest challenges in physics nowadays. A promising approach to increase the knowledge about our Universe is based on the combination of different cosmological probes tracing the Large-Scale Structure (LSS) of

the Universe, such as the cosmic microwave background (CMB) temperature anisotropies, galaxy clustering, weak gravitational lensing, galaxy-galaxy lensing and galaxy clusters.

Current surveys such as the Dark Energy Survey (DES¹), the Canada France Hawaii Telescope Lensing Survey (CFHTLenS²), the Kilo-Degree Survey (KiDS³) and the Dark Energy Spectroscopic Instrument (DESI⁴) continue to set tighter constraints on the cosmological model and its components. Future surveys such as the Legacy Survey of Space and Time (LSST⁵), Euclid⁶ and the Wide Field Infrared Telescope (WFIRST⁷) are expected to provide more and deeper data and therefore significantly advance our understanding of cosmology. Analyses based on individual cosmological probes are straightforward if they are assumed to be statistically independent [2],[3]. But since these surveys will cover large and overlapping regions of the sky, the retrieved high-quality imaging data is statistically not independent. Combining various probes in the analysis therefore allows us to consider non-negligible correlations between the probes, which have to be taken into account. Considering the cross-correlations between the statistics of the various cosmological probes not only significantly tightens the constraints on the cosmological model, but also allows us to have a better control of systematic effects and test for inconsistencies among the different probes [4]. Moreover, the increase in sensitivity of current and future CMB experiments such as Planck⁸, ACT⁹ and SPT¹⁰, allowing us to resolve CMB temperature fluctuations down to arcmin scale, could potentially lead to a correlation of the different sources of secondary CMB anisotropies with other LSS probes, such as weak gravitational lensing and the Sunyaev-Zel'dovic (SZ) effect [5] (see e.g. [6],[7],[8]).

Various earlier studies have conducted joint analyses of different cosmological probes. For example, parameter constraints from a joint analysis of galaxy-galaxy lensing and galaxy clustering have been derived in Mandelbaum *et al.* [9] and Cacciato *et al.* [10]. An extensive integrated analysis of CMB temperature anisotropies, galaxy clustering and cosmic shear has been performed in Nicola *et al.* [11] and additionally included CMB lensing maps, supernovae data and local Hubble parameter measurement data from the Hubble Space Telescope (HST) in their joint analysis in Nicola *et al.* [12].

Cosmological parameter inference not only requires the observed data vector and an accurate theoretical prediction, but also a realistic estimation of the covariance matrix Σ . The simplest approach for the latter is to use a Gaussian approximation, which gives the minimum contribution to the covariance. A Gaussian covariance matrix Σ_G would be the only contribution if the density field is a homogeneous and isotropic Gaussian random field, i.e. all information is contained in the power spectrum. The Gaussian term can then easily be computed given the survey area and the nonlinear matter power spectrum. Such an approximation for the covariance estimation is valid on sufficiently large scales (for multipoles $\ell \lesssim 100 - 200$ for galaxy sources at redshift $z_s \approx 1$ concerning cosmic shear), but becomes insufficient on smaller scales where nonlinear structure formation induces non-Gaussianities

¹<http://www.darkenergysurvey.org>

²<https://www.cfhtlens.org>

³<http://kids.strw.leidenuniv.nl>

⁴<http://desi.lbl.gov>

⁵<http://www.lsst.org>

⁶<http://sci.esa.int/euclid/>

⁷<http://wfirst.gsfc.nasa.gov>

⁸<https://www.cosmos.esa.int/web/planck>

⁹<https://act.princeton.edu/>

¹⁰<https://pole.uchicago.edu/>

in the density field [13],[14]. The non-Gaussian terms in the covariance Σ_{NG} that arise from the connected higher-order moments of the density field have been found to have a significant impact on the error bars when considering the convergence power spectrum [15], [16]. Likewise, invoking a non-Gaussian covariance matrix also significantly increases the size of the parameter constraints obtained from a Fisher matrix analysis based on the convergence power spectrum and bispectrum [17].

In contrast to using a Gaussian approximation, the evaluation of the non-Gaussian term is nontrivial. The first approach for the latter consists in directly evaluating the nonlinear matter trispectrum, which represents the analytical form of the non-Gaussian contribution to the covariance matrix [18]. Numerous analytical methods such as Standard Perturbation Theory (SPT) [18], Effective Field Theory of Large-Scale Structure (EFTofLSS) [19],[20],[21] and approaches based on the halo model [22] have been used to calculate the trispectrum. An analytical calculation of a non-Gaussian multi-probe covariance matrix based on the halo model has been calculated in Krause & Eifler [14], which incorporates cosmic shear, galaxy-galaxy lensing, galaxy clustering, cluster number counts and cluster weak lensing to perform a joint analysis using the COSMOLIKE¹¹ software.

The second common approach to evaluate the non-Gaussian term consists in generating a sufficiently large ensemble of statistically independent realizations of the matter density field, from which the power spectrum sample covariance can be measured (see e.g. [16],[23],[24],[25],[26],[27],[28],[29]). Following such an approach, recent work done in Harnois-Déraps *et al.* [30] introduced a multi-probe covariance matrix for CMB lensing, cosmic shear, galaxy-galaxy lensing and galaxy lensing from 844 independent realizations.

Combining these two approaches has led to the development of hybrid methods, which analytically compute the well-understood parts of the covariance matrix and use simulations to estimate the remaining parts [31]. A fourth approach measures simulation covariances from different subsamples of the underlying dataset, such that their combination is less affected by noise when estimating the diagonal elements of the covariance matrix [32].

The drawback of the numerical ensemble-approach is its computational cost: For each statistically independent realization of the non-Gaussian matter density field, a N -Body simulation has to be performed. This conflicts with the need of a large ensemble of realizations required to estimate a statistically well-converged covariance matrix. Future surveys are expected to measure in hundreds of data bins, which will require an order of 10^4 simulation realizations to prevent 5-10% degradation in the parameter constraints [33]. To this end, various alternative methods to fully realized N -Body codes have been developed, such as the Comoving Lagrangian Acceleration method (COLA; [34],[35]) and applications thereof (e.g. L-PICOLA [36],[37],[38],[1] and ICE-COLA [39],[40]). Although these methods are several orders of magnitude faster than full N -Body codes, they lack accuracy on small scales. Another interesting alternative method consists in reusing the same N -Body simulation output by applying random transformations to generate multiple quasi-independent maps. Concerning the cosmic shear field, it has been shown by Petri *et al.* [28] that one single N -Body output is sufficient to produce $\sim 10^4$ realizations.

This work presents an extension of the UFALCON package, which was first introduced in our paper [1] and initially designed to generate full-sky convergence maps with a minimal runtime. UFALCON has recently been applied in Kapcprzak *et al.* [41] for the covariance estimation based on the approximate N -Body code L-PICOLA. Furthermore, it was

¹¹<https://github.com/CosmoLike>

used to generate convergence maps used as training data for Convolutional Neural Networks (CNN) for cosmological parameter inference in Fluri *et al.* [42],[43],[44] and used to study non-Gaussian statistics such as peak counts, minimum counts and Minkowski functionals in Zürcher *et al.* [45]. The presented extension adds the functionality to the code to generate a complete *set* of full-sky maps for different cosmological probes, such as weak lensing shear, galaxy overdensity including the effects of redshift-space distortions (RSD), CMB lensing and CMB temperature anisotropies from the ISW effect. Furthermore, we invoke a randomization procedure based on random transformation applied to the 3-dimensional matter density field in order to enhance the number of realizations at least by a factor of ~ 20 . Our pipeline is designed to post-process output of the DM-only N -Body simulation code PKDGRAV3 (Stadel *et al.* [46]), but is in general able to use output of different N -Body codes. UFALCON applied to PKDGRAV3 output combines accuracy and minimal computational runtime: The simulation of the density field guarantees to satisfy a certain force accuracy and is therefore not an approximate N -Body code. Furthermore, the PKDGRAV3 code is highly efficient and can be run with graphics processing units (GPU) support. The subsequent post-processing with UFALCON can be parallelized on a computer cluster and has a runtime of ~ 1 hour walltime for one set of full-sky maps.

Furthermore, UFALCON offers the possibility to generate continuous full-sky CMB lensing potential and deflection angle maps directly from the gravitational potential of the density field. Our approach of using large periodic simulation volumes together with an interpolation routine enables the generation of continuous lensing potential maps which include nonlinear and non-Gaussian effects. These maps can be of use to help separating the different contributions to the CMB anisotropies and improve on an accurate and complete interpretation of the latest Planck data [47].

In this paper, we first describe the extension of the UFALCON package, namely the possibility to compute full-sky maps of different cosmological probes from the same underlying density field. We describe the application of UFALCON to the DM-only N -Body simulation output generated using the PKDGRAV3 code and the statistical analysis of the generated full-sky maps by considering the 4 auto- and the 6 cross- spherical harmonic power spectra between the probes. Furthermore, we estimate a multi-probe covariance matrix based on 630 quasi-independent realizations and perform a forecast analysis for a stage-IV-like survey geometry based on spherical harmonic power spectra for multipoles between $\ell = 10^2$ and 10^3 . Hereby we focus on quantifying the impact of including different probe-combinations, the effect of including the cross-correlations between the probes and the use of a fully non-Gaussian simulation-based covariance matrix on cosmological parameter constraints. The obtained results are compared to the case where we use a Gaussian approximation for the covariance matrix.

This paper is organized as follows. In section 2, we review the analytical framework required for our spherical harmonic power spectrum predictions. The numerical framework is discussed in section 3, which includes a description of our past-lightcone construction for the different probes and an overview of various systematic effects present. In section 4, we show various statistical quantities including a multi-probe covariance matrix we compute based on our full-sky maps. Based on our findings, we perform a forecast analysis for a stage-IV-like survey geometry in section 5 and quantify the impact of the non-Gaussian contribution to the covariance matrix on the cosmological parameter constraints.

2 Analytical Predictions

The analytical predictions for the different cosmological probes considered are calculated in the same way as in Nicola *et al.* [11] using PYCOSMO (see Réfrégier *et al.* [48], Tarsitano *et al.* [49]), which is a Python-based framework to solve the Einstein-Boltzmann equations governing the evolution of the linear perturbations. We consider the statistical properties of two probes i and j by computing the spherical harmonic power spectra C_ℓ^{ij} using the *Limber approximation* ([50],[51],[52]) at multipole ℓ given by

$$C_\ell^{ij} = \int dz \frac{c}{H(z)} \frac{W^i(\chi(z)) W^j(\chi(z))}{\chi^2(z)} P_{\delta\delta}^{\text{nl}} \left(k = \frac{\ell + 1/2}{\chi(z)}, z \right), \quad (2.1)$$

where $H(z)$ is the Hubble parameter, $\chi(z)$ the comoving distance and c is the speed of light. Note that equation (2.1) is not only used to make analytical predictions for the auto-correlations, but also for the cross-correlations between different probes. The Limber approximation has been used in order to speed up the calculation and is valid for multipoles $\ell \gtrsim 10$ (i.e. small angular scales) and broad redshift bins [11],[53]. The nonlinear matter power spectrum $P_{\delta\delta}^{\text{nl}}(k, z)$ is calculated using the fitting function from Mead *et al.* [54],[55], whereas the linear matter power spectrum is obtained from the transfer function derived by Eisenstein & Hu [56]. In the following we describe the window functions implemented in PYCOSMO for the cosmological probes $i, j \in \{\gamma, \delta_g, \kappa_{\text{CMB}}, \Delta T_{\text{ISW}}\}$, described below for a flat cosmological model. Note that UFALCON does not depend on the code used to calculate analytical predictions. The N -Body simulation-based results from our pipeline can therefore be compared to analytical predictions from other codes, such as CLASS [57].

Weak lensing shear (γ). The window function for cosmic shear is given by [11]

$$W^\gamma(\chi(z)) = \frac{3}{2} \frac{\Omega_m H_0^2}{c^2} \frac{\chi(z)}{a} \int_{\chi(z)}^{\chi_h} dz' n(z') \frac{\chi(z') - \chi(z)}{\chi(z')}, \quad (2.2)$$

where Ω_m and H_0 denote the present day values of the matter density and the Hubble parameter respectively. Furthermore, χ_h is the comoving distance to the horizon, $n(z)$ is the normalised redshift selection function of the lensed galaxies and a denotes the scale factor. Note that a simple ℓ -dependent pre-factor of the form $(\ell + 2)(\ell + 1)\ell(\ell - 1)(\ell + 0.5)^{-4}$ can be multiplied to the Limber-approximated cosmic shear power spectrum formula to alleviate some of the inaccuracies of the Limber approximation on multipoles $\ell \lesssim 10$ [58]. Since we are interested in computing the Limber approximated power spectra of different probes in a consistent way (i.e. based on equation (2.1)) and focusing our analysis on multipoles between $\ell = 100$ and 1000, we choose not to apply the pre-factor to our power spectrum calculations.

Galaxy clustering (δ_g). Regarding galaxy clustering, the window function can be written as [11]

$$W^{\delta_g}(\chi(z)) = \frac{H(z)}{c} b(z) n(z). \quad (2.3)$$

In our analysis, we use a simple approach based on a constant, linear, scale- and redshift-independent galaxy bias $b(z) \equiv b$. This is a valid assumption on large scales, which are well-described by linear theory. More complicated galaxy bias models could also be implemented. The observed galaxy redshifts are typically converted to radial distances by using Hubble's

law, which neglects the peculiar velocities of the galaxies. This leads to redshift-space distortions (RSD) between the clustering of galaxies along the line-of-sight and perpendicular to it. The true comoving position of a galaxy \vec{r} is distorted along the line-of-sight due to its peculiar velocity \vec{v} according to [59]

$$\vec{s} = \vec{r} + \frac{v_{||}(\vec{r})}{aH(a)} \hat{e}_{||}, \quad (2.4)$$

where $\hat{e}_{||}$ denotes the unit vector along the line-of-sight. We refer to [60] and [59] for a more detailed description of galaxy clustering and RSD. The above description of the power spectrum for galaxy clustering ignores the effect of the peculiar velocities of the galaxies on the nonlinear power spectrum $P_{\delta\delta}^{\text{nl}}(k, z)$. In the presence of RSD, the window function for galaxy clustering has an additional component given by [61]

$$W_{\text{RSD}}^{\delta_g} = \frac{H(z)}{c} b(z) n(z) \left[\beta \frac{(2\ell^2 + 2\ell - 1)}{(2\ell + 3)(2\ell - 1)} - \beta \frac{\ell(\ell - 1)}{(2\ell - 1)(2\ell + 1)} - \beta \frac{(\ell + 1)(\ell + 2)}{(2\ell + 1)(2\ell + 3)} \right], \quad (2.5)$$

where $\beta \approx \Omega_m^{0.6}/b(z)$ is the approximated redshift distortion parameter. Note that the additional term vanishes in the limit of $\ell \gg 1$, i.e. $W_{\text{RSD}}^{\delta_g} \xrightarrow{\ell \gg 1} 0$, and mostly contribute to the largest scales ($\ell \lesssim 30$). We refer to [61] for a detailed derivation of the window function for galaxy clustering in presence of RSD.

CMB temperature anisotropies (ΔT). The spherical harmonic power spectrum of the temperature anisotropies T of the CMB can be related to the primordial power spectrum generated during inflation $P_{\delta\delta}^{\text{lin}}(k)$ and is given by [62]

$$C_\ell^{TT} = \frac{2}{\pi} \int dk k^2 P_{\delta\delta}^{\text{lin}}(k) \left| \frac{\Delta T_\ell(k)}{\delta(k)} \right|, \quad (2.6)$$

where $\Delta T_\ell(k)$ represents the CMB temperature anisotropies, $\delta \equiv (\rho - \bar{\rho})/\bar{\rho}$ is the density contrast and $\bar{\rho}$ the mean density of the universe. Secondary temperature perturbations in the CMB radiation can be generated by the linear (integrated Sachs-Wolfe or ISW effect [63]) and nonlinear (Rees-Schiama or RS effect [64]) decay of large-scale gravitational potential fluctuations. These temperature fluctuations arising from the ISW + RS effect can be written as the integral over conformal time η of the time derivative of the gravitational potential ([65],[63],[66])

$$\Delta T_{\text{ISW}}(\hat{n}) = T_{\text{CMB}} \delta T_{\text{ISW}} = 2 T_{\text{CMB}} \int_{\eta_r}^{\eta_0} d\eta \frac{\partial \Phi}{\partial \eta}, \quad (2.7)$$

where η_0 and η_r represents the conformal time today and at recombination respectively. CMB temperature anisotropies are correlated through the ISW effect to tracers of the LSS such as weak lensing shear or galaxy clustering [63]. In the present work, we focus on the temperature anisotropies due to the ISW effect ΔT_{ISW} .

This source of secondary CMB anisotropies is especially challenging to measure, since the ISW signal suffers from cosmic variance at large scales and is entangled with the nonlinear RS signal at smaller scales. A disentanglement between the two signals at smaller scales is thus crucial to correctly retrieve cosmological information [67]. On larger scales, where

linear theory holds, the spherical harmonic power spectrum between the CMB temperature anisotropies and a tracer $i \in \{\gamma, \delta_g, \kappa_{\text{CMB}}\}$ of the LSS can be written as [68]

$$C_\ell^{iT} = T_{\text{CMB}} \left(\frac{3\Omega_m H_0^2}{c^2} \right) \frac{1}{(\ell + 1/2)^2} \int dz \frac{d}{dz} [D(z)(1+z)] \times D(z) W^i(\chi(z)) P_{\delta\delta}^{\text{lin}} \left(k = \frac{\ell + \frac{1}{2}}{\chi(z)}, 0 \right), \quad (2.8)$$

where the window function $W^i(\chi(z))$ is given by equation (2.2), (2.3) or (2.13). The linear matter power spectrum $P_{\delta\delta}^{\text{lin}}(k, z)$ has been split up into a time-dependent growth factor $D(z)$ and a scale-dependent part $P_{\delta\delta}^{\text{lin}}(k, 0)$ [11]. Furthermore, the mean temperature of the CMB today is denoted by T_{CMB} . A detailed derivation of equation (2.8) for galaxy clustering and weak lensing shear can be found in Padmanabhan *et al.* [65] and Appendix F in Nicola *et al.* [11] respectively.

We additionally implemented the auto-correlation of the temperature anisotropies from the ISW effect ΔT_{ISW} in order to verify more directly our results obtained from the numerical N -Body simulation, which can be written as

$$C_\ell^{\text{ISW}} = T_{\text{CMB}}^2 \left(\frac{3\Omega_m H_0^2}{c^2} \right)^2 \frac{1}{(\ell + 1/2)^4} \int dz \frac{d}{dz} [D(z)(1+z)]^2 \chi(z)^2 \times P_{\delta\delta}^{\text{lin}} \left(k = \frac{\ell + 1/2}{\chi(z)}, 0 \right). \quad (2.9)$$

A derivation of equation (2.9) is given in Appendix A. In the present work we consider the ΔT_{ISW} auto-correlation and all 3 cross-correlations between ΔT_{ISW} and the tracers $\{\gamma, \delta_g, \kappa_{\text{CMB}}\}$ of LSS. The cross-correlations between the CMB temperature anisotropies and the galaxy overdensity and weak lensing shear are mainly due to the ISW effect [63]. As pointed out in [12], the cross-correlation between the CMB temperature anisotropies and the CMB lensing convergence is also mostly dominated by the ISW effect but additionally obtains contributions from the Sunyaev-Zel'dovic effect (SZ) [69] and the Doppler effect due to the bulk velocities of electrons scattering the CMB photons (see e.g. [70] and [71] for more details). We do not take into account these further contributions in the present analysis.

CMB lensing (κ_{CMB}). The CMB can be described by primary anisotropies imprinted on the last scattering surface and by secondary anisotropies, which originate from the scattering of the CMB photons by matter inhomogeneities and on electrons along the way to us. Amongst the most important effects leading to secondary anisotropies is the weak gravitational lensing of the CMB, which arises from the deflection of CMB photons through potential gradients along our line of sight [72].

In the subsequent discussion, we approximate recombination as an instantaneous process at redshift $z_* \approx 1100$ located at a single source plane at a comoving distance $\chi_* \approx 1.5 \times 10^4$ Mpc. Working with conformal time η in a flat universe, we define the lensing potential (induced by scalar perturbations with no anisotropic stress) as a function of the line-of-sight pointing in direction $\hat{n} = (\theta, \phi)$ as [73], [74]

$$\psi(\hat{n}) = -2 \int_0^{\chi_*} \frac{\chi_* - \chi}{\chi_* \chi} \frac{\Phi(\chi \hat{n}; \eta_0 - \chi)}{c^2} d\chi, \quad (2.10)$$

where $\eta_0 - \chi$ corresponds to the conformal time at which the photon was at comoving coordinates $\chi\hat{n}$ and Φ is the physical peculiar gravitational potential generated by matter inhomogeneities. The deflection angle of a source located at χ_* is given in terms of the lensing potential as

$$\alpha(\hat{n}) = -2 \int_0^{\chi_*} \frac{\chi_* - \chi}{\chi_* \chi} \nabla_{\hat{n}} \frac{\Phi(\chi\hat{n}; \eta_0 - \chi)}{c^2} d\chi, \quad (2.11)$$

with $\nabla_{\hat{n}}$ representing the divergence operator on the sky, i.e. the two-dimensional derivative transverse to the direction \hat{n} (see e.g. [72],[75],[76],[77]). The scalar spherical harmonic coefficients of the CMB lensing potential $\psi_{\text{CMB},\ell m}$ are related to the CMB lensing convergence $\kappa_{\text{CMB},\ell m}$ through [78]

$$\kappa_{\text{CMB},\ell m} = \frac{\ell(\ell+1)}{2} \psi_{\text{CMB},\ell m}. \quad (2.12)$$

As described in [12], the window function for the CMB lensing convergence can be expressed as the single-plane limit of the weak lensing shear window function (equation (2.2)) and be written as

$$W^{\kappa_{\text{CMB}}}(\chi(z)) = \frac{3}{2} \frac{\Omega_m H_0^2}{c^2} \frac{\chi(z)}{a} \frac{\chi(z_*) - \chi(z)}{\chi(z_*)}. \quad (2.13)$$

3 Numerical Methods

The UFALCON pipeline was first introduced in [1] and designed to generate full-sky convergence maps for weak lensing shear. In this section, we describe the novel extension to UFALCON, which includes the functionality to generate a complete set of full-sky maps for the cosmological probes γ , δ_g , κ_{CMB} and ΔT_{ISW} from the same N -Body simulation output. We describe the underlying N -Body simulation, the lightcone construction and the map-making procedure for the different probes. We further highlight the construction of CMB lensing potential maps ψ_{CMB} and the deflection angle α from first principles. Moreover, we give a short description of the publicly available UFALCON package, which contains the weak gravitational lensing part of the pipeline.

3.1 N-Body Simulation

As of now, N -Body simulations provide the most accurate method to predict a wide dynamical range of structure formation. In the context of current and future LSS surveys, smaller angular scales indeed need to be under control in order to correctly infer cosmological parameters. We use the DM-only N -Body code PKDGRAV3 (Stadel *et al.* [46]) to simulate the matter density field. PKDGRAV3 is based on the Fast Multipole Method (FMM) to accurately compute the forces between the particles and scales as $\mathcal{O}(N)$. Furthermore, it is highly optimised for usage on the Piz Daint supercomputer (CSCS¹², Switzerland) and can be further accelerated when run with graphics processing unit (GPU) support. PKDGRAV3 has been successfully run with more than a trillion particles in Potter *et al.* [79] and used as training data for CNN's used for cosmological inference [44].

Simulation configuration. In this study, we assume a flat Λ CDM cosmological model with fiducial parameter values given by

$$\theta_{\text{fid}} = \{h, \Omega_m, \Omega_b, n_s, \sigma_8, T_{\text{CMB}}\} = \{0.7, 0.3, 0.05, 0.961, 0.8, 2.275 \text{ K}\}. \quad (3.1)$$

¹²<https://www.cscs.ch/>

We aim at accurately resolving angular scales corresponding to multipoles between $\ell = 10^2$ and 10^3 , which imposes the need to have a sufficiently high resolution in the simulation to include the effects of nonlinear structure formation. At the same time, we need a sufficiently large simulation volume in order to incorporate large scale perturbation modes (see section 3.3.2 for a discussion of super-sample covariance effects) and to cover an appropriate redshift range. We therefore ran a total of 30 simulations with $N_p = 1024^3$ particles in a volume of $V_{\text{sim}} = (1600 \text{ Mpc})^3$ (with a mass per DM-particle of $3.43 \times 10^{11} M_\odot$). Each simulation was generated with a different random seed for the initial conditions at redshift $z_{\text{init}} = 50$ using the initial conditions generator MUSIC [80]. Note that the redshift-interval between the outputs of the simulation is not constant and is defined by the choice of z_{init} , z_{final} , the number of timesteps and the cosmological parameters. The simulations were subsequently run with 150 timesteps between $z_{\text{init}} = 50$ and $z_{\text{final}} = 0.0$, with more outputs for lower redshifts. The simulation outputs a snapshot at every timestep. We store and post-process 54 snapshots output between redshift $z = 0.0$ to 1.75 using UFALCON. Although the redshift-interval between the outputs is not constant, we have a mean redshift-spacing of about ~ 0.03 in the interval of our interest. We set the accuracy parameters given by the tree opening angles for different redshifts to the default values $\theta = 0.4$ for $z > 20$, $\theta_{20} = 0.55$ for $20 > z > 2$ and $\theta_2 = 0.7$ for $2 > z$. The force calculation in PKDGRAV3 is realized through particle-particle and particle-cell interactions. Choosing a smaller value of θ results in a larger tree opening radius and more particle-particle interactions are calculated, while a high value of θ results in less particle-particle interactions. At very early times ($z > 20$), when the Universe is very homogeneous, a smaller value of θ is necessary to obtain a certain accuracy in the force calculation. Otherwise, small errors in the initial nonlinear growth at early times could be amplified during the evolution and potentially lead to errors greater than 1% in the power spectrum at the end of the simulation [46],[79].

Runtime. The above simulation configuration leads to a walltime-runtime of about ~ 2 hours for lightcone-output (i.e. one output-file containing the particles at different redshifts, concentrically arranged) and ~ 4 hours (~ 32 node-hours) for snapshot output per simulation with GPU-support on our computer cluster.

3.2 Lightcone Construction

Our aim is to generate full-sky maps covering a redshift range from $z = 0.0$ to 1.75, i.e. we have to construct a lightcone spanning a large survey volume. To this end, we decided to adopt a replication scheme in order to guarantee a sufficiently high resolution of the simulated density field across the full survey volume. Note that in our first paper [1], we adopted an alternative lightcone-construction scheme by nesting two simulation boxes with different volumes and resolutions.

We replicate the simulation volume 6 times in x , y and z direction, leading to a total of 216 replicas for the whole volume. The lightcone is constructed by concentrically stacking shells at different redshift of the replicated density field around the observer located at $z = 0$. A sketch of the lightcone construction is shown in Figure 1. To construct our maps we make use of the Hierarchical Equal Area Iso-Latitude Pixelization tool¹³ (HEALPIX) [81] to pixelize the sphere with a resolution of $n_{\text{side}} = 1024$. In order to construct full-sky maps for weak lensing shear, CMB lensing convergence and galaxy overdensity we project the integrand in

¹³<http://healpix.sourceforge.net>

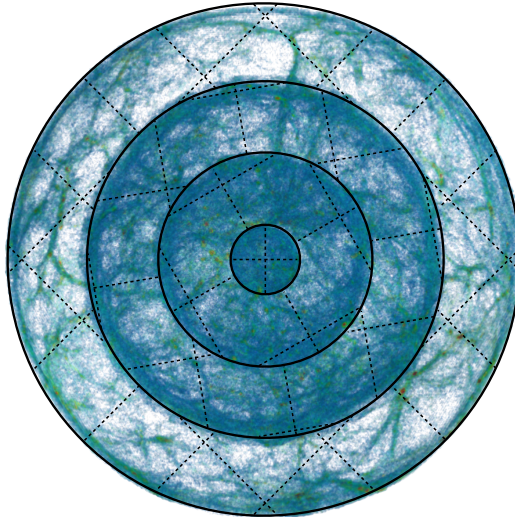


Figure 1: Sketch of the full-sky lightcone construction obtained by replicating the density field. The simulation output at a discrete number of redshifts are used to generate concentrically arranged shells around the observer located at the center. The shell randomisation procedure, here depicted by the different orientation of the simulation volume (dashed lines) in each shell, is described in section 3.3.4.

radial direction. On the other hand, the temperature anisotropies maps from the ISW effect and the CMB lensing potential maps are constructed by interpolating the density field and integrating the quantity along each ray. Importantly, the different maps are constructed from the same underlying density field, such that when computing the spherical harmonic power spectra, one can consider the auto- *and* the cross-correlations between the different probes.

Runtime. Our pipeline works by parallelising the processing of the simulation output (i.e. each snapshot-output is processed simultaneously) and takes ~ 1 hour walltime (~ 100 CPU-hours) to generate one set of full-sky maps when run on a CPU-based computer cluster.

3.2.1 Projected Lightcone

Convergence. The following treatment is based on the *Born approximation*, which is valid when the change in the comoving separation between the light rays, being deflected through gravitational lensing, is small compared to the comoving separation between undeflected light rays (i.e. the *small-angle scattering limit*). As detailed in [1], we follow the procedure described in the Appendix A of [82]. The convergence value of a given pixel θ_{pix} is thus given by

$$\kappa(\theta_{\text{pix}}) \approx \frac{3}{2} \Omega_m \sum_b W_b \frac{H_0}{c} \int_{\Delta z_b} \frac{cdz}{H_0 E(z)} \delta \left(\frac{c}{H_0} \mathcal{D}(z) \hat{n}_{\text{pix}}, z \right), \quad (3.2)$$

where \hat{n}_{pix} is the unit vector pointing to the center of the pixel and the dimensionless comoving distance is given by $\mathcal{D}(z) = (H_0/c)\chi(z)$. The sum in equation (3.2) runs over all the timesteps with simulation output (i.e. redshift-shell with index b) between $z = 0.0$ to 1.75 . The integral over the density contrast can be recast as a function of the number of particles n_p in shell b

with thickness $\Delta\chi_b$ located in pixel θ_{pix} , giving a practical expression for the convergence [1]

$$\kappa(\theta_{\text{pix}}) \approx \frac{3}{2} \Omega_m \sum_b W_b \left(\frac{H_0}{c} \right)^3 \frac{N_{\text{pix}}}{4\pi} \frac{V_{\text{sim}}}{N_p} \frac{n_p(\theta_{\text{pix}}, \Delta\chi_b)}{\mathcal{D}^2(z_b)}, \quad (3.3)$$

where N_{pix} is the total number of pixels on the sky. Each shell $\Delta\chi_b$ is multiplied with a weight W_b , which depends on the redshift distribution of the source galaxies. For an arbitrary redshift distribution $n(z)$, the weights can be written as

$$W_b^{n(z)} = \left(\int_{\Delta z_b} \frac{dz}{E(z)} \int_z^{z_s} dz' n(z') \frac{\mathcal{D}(z) \mathcal{D}(z, z')}{\mathcal{D}(z')} \frac{1}{a(z)} \right) / \left(\int_{\Delta z_b} \frac{dz}{E(z)} \int_{z_0}^{z_s} dz' n(z') \right), \quad (3.4)$$

where $\mathcal{D}(z, z') = \mathcal{D}(z') - \mathcal{D}(z)$. We used equation (3.4) together with a source galaxy distribution based on Smail *et al.* [83] given by

$$n(z) = z^\alpha e^{-(z/z_s)^\beta}, \quad (3.5)$$

where $\alpha = \beta = 2.0$, $z_s = 0.7$ and normalized it to unity, i.e. $\int dz n(z) = 1$. The full-sky convergence maps we obtained have then been converted to weak lensing shear maps using [78],

$${}_2\gamma_{\ell m} = \frac{-1}{\ell(\ell+1)} \sqrt{\frac{(\ell+2)!}{(\ell-2)!}} \kappa_{\ell m}, \quad (3.6)$$

where ${}_2\gamma_{\ell m}$ are the spin-2 spherical harmonic coefficients of the weak lensing shear. In order to compute the CMB lensing convergence field from equation (3.3), we use the weights

$$W_b^{z_s} = \left(\int_{\Delta z_b} \frac{dz}{E(z)} \frac{\mathcal{D}(z) \mathcal{D}(z, z_s)}{\mathcal{D}(z_s)} \frac{1}{a(z)} \right) / \left(\int_{\Delta z_b} \frac{dz}{E(z)} \right), \quad (3.7)$$

with a single source located at $z_s = z_*$.

Galaxy clustering. Analogously to the expression for the convergence given by equation (3.3) and the approximations described in section 2, we can approximate the galaxy clustering by

$$\delta_g(\theta_{\text{pix}}) \approx \sum_b W_b^{\delta_g} \left(\frac{H_0}{c} \right)^2 \frac{N_{\text{pix}}}{4\pi} \frac{V_{\text{sim}}}{N_p} \frac{n_p(\theta_{\text{pix}}, \Delta\chi_b)}{\mathcal{D}^2(z_b)}, \quad (3.8)$$

where the weights are given by

$$W_b^{\delta_g} = \left(\int_{\Delta z_b} \frac{dz}{E(z)} H(z) b(z) n(z) \right) / \left(\int_{\Delta z_b} \frac{dz}{E(z)} \right). \quad (3.9)$$

Full-sky maps for galaxy clustering are constructed by projecting the particles within each redshift-shell (no. of particles in shell b given by $n_p(\Delta\chi_b)$) onto the sky, before weighting and summing up the shells over the full lightcone. Taking into account the peculiar velocities of the individual particles $v_{||}$, we can alter the positions of the particles in radial direction due to RSD (no. of particles in shell b due to RSD given by $n_p^{\text{RSD}}(\Delta\chi_b)$). Therefore, in our lightcone construction pipeline, the magnitude of the RSD effect depends on the thickness of the redshift shells. The thinner the shell, the more likely it is that a particle changes the shell and is associated to a different redshift. Note that shells closer to the observer are thinner and provide therefore a better resolution for the lightcone construction (see section 3.3.1). In Figure 2 we show one realisation of the full-sky maps κ_{smail} , κ_{CMB} , δ_g and ΔT_{ISW} , where κ_{smail} represents the convergence field based on a source galaxy distribution given by equation (3.5).

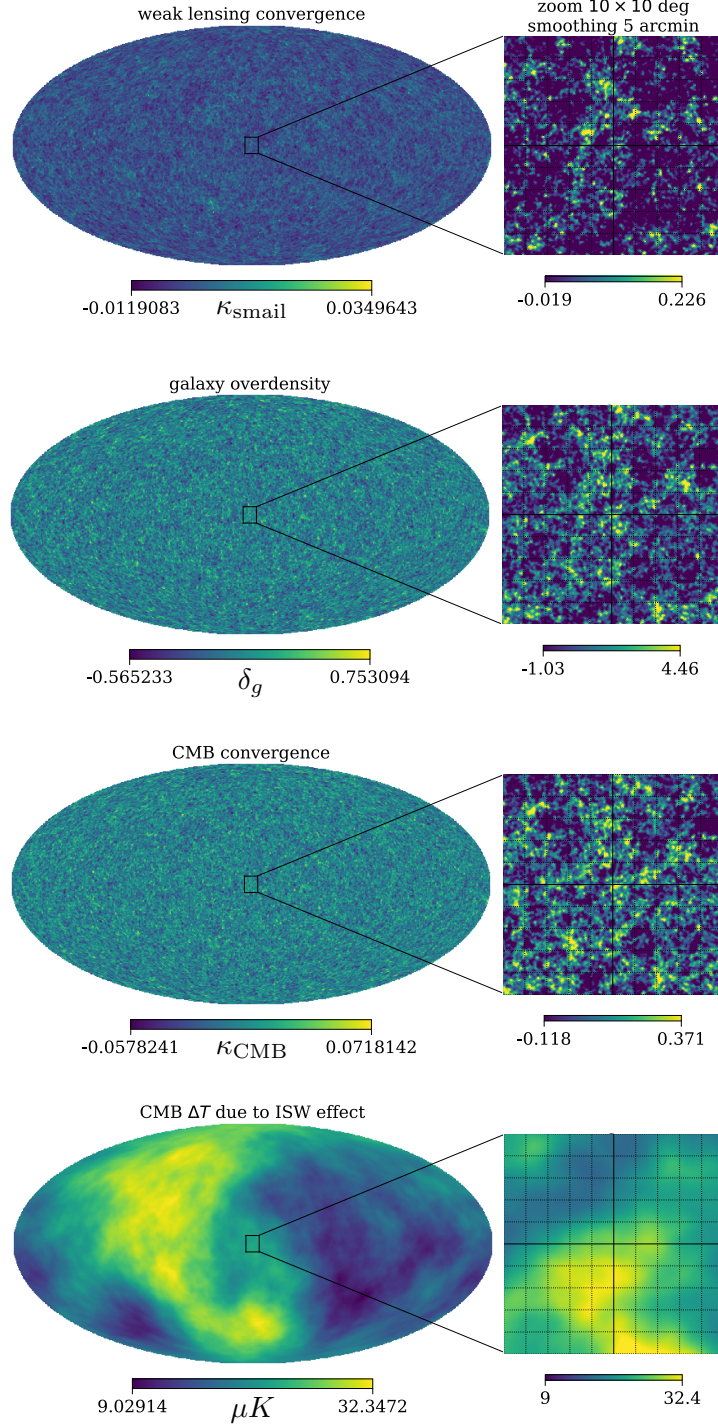


Figure 2: Full-sky maps generated from one N -Body realization for $z = 0.0 - 1.75$. From top to bottom: (a) Weak lensing convergence map based on a Smail *et al.* redshift distribution. (b) Galaxy clustering map including RSD based on the DM density field. (c) CMB convergence map. (d) ΔT_{ISW} map obtained by interpolating the density field and evaluating for each pixel on the sphere. The zoom-in regions span $\sim 100 \text{ deg}^2$, have been smoothed using a Gaussian kernel with a FWHM of 5 arcmin and increased in contrast.

3.2.2 Interpolated Lightcone

In this section, we present our procedure based on Cai *et al.* [67] and Smith *et al.* [84] to construct full-sky maps of the temperature fluctuations from the ISW effect and the CMB lensing potential from our simulations which are *continuous* on the sky. We first construct an estimate of Φ and $\dot{\Phi}$ on a cubic grid, interpolate the quantity and integrate ψ_{CMB} and ΔT_{ISW} respectively along each ray of the past-lightcone.

ISW effect. The integral in equation (2.7) can be rewritten as a function of comoving distance as

$$\Delta T_{\text{ISW}}(\hat{n}) = \frac{2}{c^3} \int_0^{\chi_*} \dot{\Phi}(\chi \hat{n}; \eta_0 - \chi) a d\chi. \quad (3.10)$$

We use Poisson's equation in comoving coordinates $\nabla^2 \Phi(\vec{x}, t) = 4\pi G \bar{\rho}(t) a^2 \delta(\vec{x}, t)$ to write the gravitational potential in Fourier space given by

$$\Phi(\vec{k}, t) = -\frac{3}{2} \left(\frac{H_0}{k} \right)^2 \Omega_m \frac{\delta(\vec{k}, t)}{a}. \quad (3.11)$$

The time derivative of $\Phi(\vec{k}, t)$ together with the Fourier space form of the continuity equation $\dot{\delta}(\vec{k}, t) + i \vec{k} \cdot \vec{p}(\vec{k}, t) = 0$ can be written as

$$\dot{\Phi}(\vec{k}, t) = \frac{3}{2} \left(\frac{H_0}{k} \right)^2 \Omega_m \left[\frac{H(a)}{a} \delta(\vec{k}, t) + \frac{i \vec{k} \cdot \vec{p}(\vec{k}, t)}{a} \right], \quad (3.12)$$

where $\vec{p}(\vec{k}, t) = [1 + \delta(\vec{k}, t)] \vec{v}(\vec{k}, t)$ is the momentum density. Equation (3.12) contains the contributions from the linear ISW effect as well as the non-linear RS effect and relates the evolution of the gravitational potential to the time-evolution of the matter fluctuations. In order to isolate the linear ISW effect, one can work in the linear regime and use $\dot{\delta}(\vec{k}, t) = \dot{D}(t) \delta(\vec{k}, z=0)$, where $D(t)$ is the linear growth factor. In this case, equation (3.12) can be rewritten as

$$\dot{\Phi}(\vec{k}, t) = \frac{3}{2} \left(\frac{H_0}{k} \right)^2 \Omega_m \frac{\dot{a}}{a^2} \delta(\vec{k}, t) [1 - \beta(t)], \quad (3.13)$$

where the linear growth rate is given by $\beta(t) \equiv d \ln D(t) / d \ln a$. Here the overdensity field directly determines the potential field and its time derivative.

The quantity $\dot{\Phi}(\vec{k}, t)$ given by equation (3.13) is then constructed as follows: First, we use a cloud-in-cell mass assignment scheme (CIC) [85] to obtain the density field $\delta(\vec{x})$ on a 3D cubic grid with 1024^3 cells. The density field is then Fast Fourier transformed to compute $\dot{\Phi}$ in Fourier space. Second, we perform an inverse Fourier transform to obtain $\dot{\Phi}(\vec{x})$ and interpolate linearly. Lastly, we approximate the integral given by equation (3.10) as a sum over discrete set of steps in comoving radial distance

$$\Delta T_{\text{ISW}}(\theta_{\text{pix}}) = \frac{2}{c^2} \sum_{b, \delta z} \dot{\Phi}(\chi \hat{n}_{\text{pix}}, z) a \Delta \chi, \quad (3.14)$$

where the steps are given by $\Delta \chi = \chi(z_b + \delta z) - \chi(z_b)$ and we use a finer redshift-spacing $\delta z = 0.01$ within each shell Δz_b related to the timesteps of the simulation. We then evaluate ΔT_{ISW} for all the rays pointing to the center of the $12 \times \text{nside}^2$ pixels of our map. In the bottom panel of Figure 2 we show a full-sky map of ΔT_{ISW} .

CMB lensing potential. Full-sky maps of the lensing potential of the CMB can be computed using equation (2.10). Therefore, we can directly use the gravitational potential field Φ output from the PKDGRAV3 simulation or compute it from the overdensity field δ by solving Poisson’s equation. The following discussion is based on using Φ directly from the simulation. Analogously to the construction of the ΔT_{ISW} maps described above, we use a CIC mass assignment scheme to get the gravitational potential on a 3D cubic grid with 1024^3 cells. The Φ -field is then interpolated linearly and the expression given by equation (2.10) is approximated by a sum over discrete steps corresponding to a redshift-spacing of $\delta z = 0.01$ (analogous to equation (3.14)). In order to integrate over all the redshifts relevant for CMB lensing, one needs to cover a large enough volume. In the present work, we replicate the simulation volume 6 times along each axis, reaching a redshift of $z \sim 1.75$. According to Carbone *et al.* [74], a contribution to the lensing power from redshifts higher than $z \sim 11.22$ is negligible for the lensing of CMB photons. For our setup this would suggest to double the number of replications along each axis, which is computationally more expensive. Figure 3 shows our results for full-sky maps of the CMB lensing potential and the corresponding deflection angle modulus $|\vec{\alpha}| = \sqrt{(\Delta\theta)^2 + (\Delta\phi)^2}$ (see Appendix E for a discussion of CMB lensing).

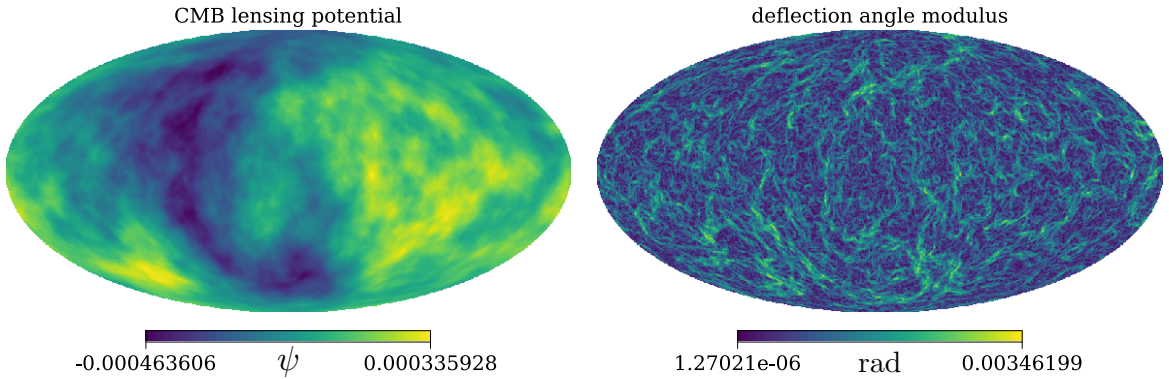


Figure 3: Left panel: Full-sky CMB lensing potential map obtained by interpolating the density field and evaluating for each pixel on the sphere for $z = 0.0 - 1.75$. Right panel: Corresponding map of the deflection angle modulus $|\vec{\alpha}| = \sqrt{(\Delta\theta)^2 + (\Delta\phi)^2}$, given by the angular derivative of the lensing potential map.

3.3 Systematic Effects

3.3.1 Simulation Resolution

PKDGRAV3 is a mesh-less tree-code, such that one can not directly infer the resolution of the simulation by considering the mean particle separation. In this case the minimally resolved scale depends on the number of particles and can be inferred by looking at the spherical harmonic power spectrum after the subtraction of the shot-noise contribution (see section 3.3.3 for a discussion of shot noise). For our simulation setup we are able to resolve angular scales within 2% compared to the analytical prediction up to $\ell \sim 1500$. Increasing the number of particles by keeping the same simulation volume would enable the resolution of even smaller scales. Eventually, this would require using a higher n_{side} -value in order to decrease the pixel size and therefore obtain a better map resolution. A comparison of our results for the spherical

harmonic power spectra using our simulation setup with analytical predictions are presented in section 4.2.

These considerations are altered when constructing maps of the temperature fluctuations from the ISW effect. In this case we first assign the overdensity to a cubic grid with 1024^3 grid cells before integrating ΔT_{ISW} given by equation (3.10). For our simulation volume with a side length of 1.6 Gpc, we are able to resolve structures down to ~ 1.6 Mpc. The resolution of our grid and the redshift-steps for the integration can have an impact on the resolution of our ΔT_{ISW} maps. Our HEALPIX maps with $n_{\text{side}} = 1024$ have a pixel size of $3.43'$ and correspond to the linear size of our grid cell at a radial comoving distance of 1120 Mpc, i.e. at a redshift of $z \sim 0.28$. We therefore expect not to compromise the resolution of the maps beyond this redshift with our choice of number of grid cells.

We have further investigated the impact of the number of timesteps used in the simulation, which determines the thickness of the redshift shells Δz_b in the lightcone construction. The N -Body simulation code PKDGRAV3 relies on adaptive time stepping, which ensures a certain time-resolution of the simulation by automatically increasing the number of substeps when choosing a lower number of timesteps (see subsection 3.2 in Potter *et al.* 2017 [79]). Therefore, as long as we use a minimum of about ~ 100 timesteps, we obtain an accurate simulation output. The number of timesteps is therefore mostly used for the number of snapshot output files, which can be postprocessed using UFALCON.

Concerning the lightcone construction using UFALCON, we observed only marginal improvements in our power spectrum results when choosing redshift shells finer than 0.05. Increasing the number of timesteps from 150 ($\Delta z_b \sim 0.03$) to 200 ($\Delta z_b \sim 0.02$) between z_{init} and z_{final} only marginally changed our power spectrum results by $\lesssim 1\%$. Choosing an even higher number of timesteps (e.g. 500 or 1500), we observe nearly zero improvements ($\ll 1\%$) in the agreement between our simulation results and the analytical predictions.

3.3.2 Super-Sample Covariance Effects

The finite volume of our simulation box can introduce systematic errors on the power spectrum, caused by missing modes larger than the simulation volume and their coupling to small-scale modes. This effect introduces an additional super-sample covariance term Σ_{SSC} to the covariance matrix [86]. According to Schneider *et al.* [87], the error on the matter power spectrum when using a box with a length of $L = 512 h^{-1} \text{Mpc}$ compared to $L = 1024 h^{-1} \text{Mpc}$ is within 1% for the wavenumbers between $k = 10^{-2} h \text{Mpc}^{-1}$ and $10^1 h \text{Mpc}^{-1}$. Considering our choice of box-length given by $L = 1120 h^{-1} \text{Mpc}$, we expect the errors to lie well within 1% for the same scales. We examined the finite volume effects on the spherical harmonic power spectrum of our full-sky maps constructed by replicating the simulation box (described in section 3) and observed a significant drop in power for very large scales $\ell \lesssim 10$ for all the probes considered. Note that such a lack of power on large scales could also stem from the underlying PKDGRAV3 code, which is a mesh-less tree-code and interpolates very large scales. Since the present forecast analysis is focused on scales between $\ell = 10^2$ and 10^3 , we leave investigations of this effect to future work.

3.3.3 Shot Noise Estimation

Particle simulations in general contain a certain amount of shot noise due to the finite number of particles involved, which can be statistically described by a Poisson distribution. Concerning the matter power spectrum, one can write the shot noise contribution as $P_{\text{sn}} = V_{\text{sim}}/N_p$ [87]. In this section we investigate the shot noise contribution to the spherical harmonic power

spectrum. The most direct approach is to use the shot noise contribution to the matter power spectrum P_{sn} and perform the weighted integrals given by equations (2.1), (2.8) and (2.9), all based on the Limber approximation [88]. The expression for the shot noise on the weak lensing convergence power spectrum is then given by

$$C_{\ell}^{\text{sn, Limber}} = \int dz \frac{c}{H(z)} \frac{W^{\kappa}(\chi(z)) W^{\kappa}(\chi(z))}{\chi^2(z)} \frac{V_{\text{sim}}}{N_p}, \quad (3.15)$$

where the integration is done using PYCOSMO. In order to relate the shot noise contribution to our numerical results more accurately, we estimate the shot noise based on the Born approximation, i.e. in a way analogous to the lightcone construction used in UFALCON. The shot noise for the weak lensing convergence can then be written as a weighted sum over the number of particles in redshift-shell b as

$$C_{\ell}^{\text{sn, Born}} = \left[\frac{3}{2} \Omega_m \left(\frac{H_0}{c} \right)^3 \frac{1}{4\pi} \right]^2 \sum_b \left[W_b \frac{V_b}{\mathcal{D}^2(z_b)} \right]^2 \frac{4\pi}{N_b}, \quad (3.16)$$

where N_b is the expected number of particles in the shell b and can be expressed as

$$N_b = \frac{N_p^{\text{sim}}}{V_{\text{sim}}} V_b. \quad (3.17)$$

A derivation of equation (3.16) is given in Appendix B, where we compare the shot noise contribution to the weak lensing convergence power spectrum based on the Limber and Born approximations. The shot noise estimates based on both approximations become equal in the limit of infinitesimal shell-thickness. We observe that the shot noise contributions using the Limber approximation and using the PKDGRAV3 redshift-spacing have the same order of magnitude and both are 2-3 orders of magnitude smaller in amplitude than our UFALCON results (see Figure 16 in Appendix B). So the choice of method does not have an impact on our final results. We therefore use the Limber approximation for the estimation of the shot noise contribution.

3.3.4 Shell Randomization Procedure

As sketched in Figure 1, we adopt a randomization scheme to increase the number of realizations from one underlying simulation run. Similarly to Carbone *et al.* [74], we apply random operations to the particle positions or to the δ and Φ fields on the 3D grids consisting of rotations by 90° (interchanging the axes), translations and parity flips [89]. Such a randomization of the simulation boxes avoids the repetition of the same structures present in the density field along the line of sight. We bundle neighbouring shells corresponding to adjacent output-redshifts together to have a thickness of about $dz \sim 0.1$. In this way we avoid breaking correlations within the density field on scales smaller than the comoving distance $\chi(z + dz) - \chi(z)$. Note that different shell-bundles are randomized using different random operations and are therefore uncorrelated. With our choice of shell-bundle we observe a loss of power of about 2% at $\ell \sim 100$ when considering the spherical harmonic power spectrum of weak lensing shear after construction of the full lightcone (left hand side of Figure 4). Importantly, all replicated boxes within one shell-bundle are randomized in a coherent way leading to a 3D tessellation (see Figure 1). This procedure conserves the continuity of the density field across the boundaries of the replicated boxes, which is particularly important to obtain continuous maps of the CMB temperature fluctuations and lensing potential across the sky.

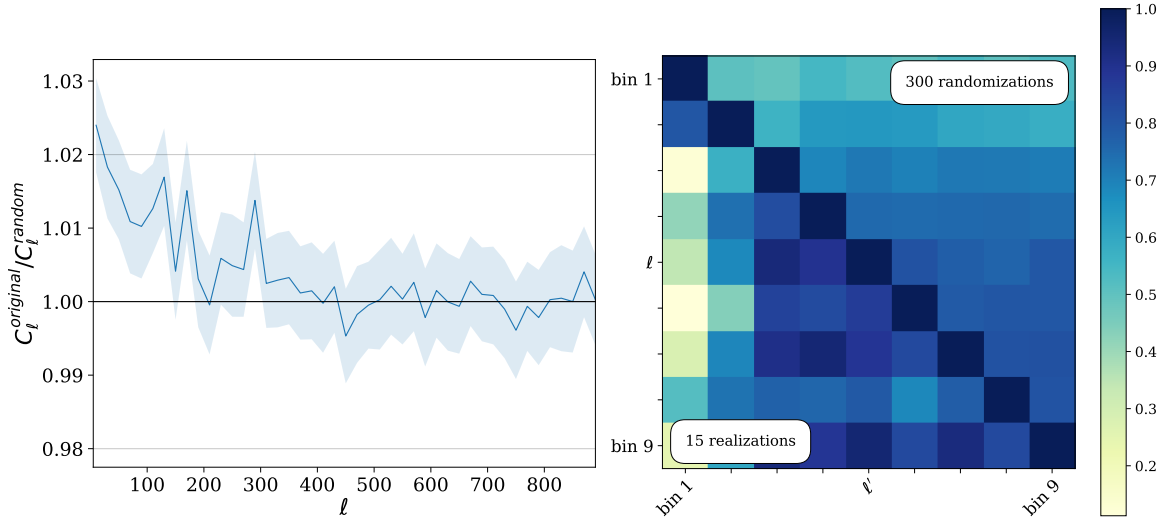


Figure 4: Left panel: Ratio between the weak lensing shear power spectrum of 15 individual simulation runs and 300 new randomized realizations between $\ell = 10^2$ and 10^3 . The choice of our shell-bundle thickness leads to a loss of power in the new realizations up to 2% at $\ell \sim 100$. Right panel: Lower triangle: Unconverged correlation matrix of weak lensing power spectrum binned between $\ell = 10^2$ and 10^3 with $\delta\ell = 100$ from 15 simulation runs only. Upper triangle: More converged correlation matrix by using 300 randomized realizations.

In the present work, we randomize each individual simulation run 20 times in order to increase the number of realizations for the covariance matrix estimation. On the right hand side of Figure 4, we show two different triangles of the correlation matrices for the weak lensing shear power spectrum binned between $\ell = 10^2$ and 10^3 with a bin-width of $\delta\ell = 100$: The lower triangle shows the unconverged correlation matrix for only 15 simulations runs. On the upper triangle, we show a more converged correlation matrix computed using the 20 new randomized realizations from the 15 individual runs.

3.3.5 Further Effects

Born approximation. The lightcone construction in our pipeline is based on the Born approximation, i.e. only the lowest-order expansion of the gravitational potential is used to compute the convergence. In this way the convergence field is integrated and weighted along the unperturbed light-rays. This stands in contrast to the fully ray-traced computation of the convergence, where the exact solution to Poisson’s equation is needed and higher order terms in Φ are included. Depending on the considered statistics and angular scales, using the Born approximation can have a non-negligible impact on cosmological parameter constraints [90].

Depending on the shape of the lensing kernel, the galaxy and CMB lensing convergence power spectra can be affected differently by the post-Born corrections. For CMB lensing the contributions could be relatively much more important than for galaxy lensing, since the CMB lensing kernel is broadly peaked at high redshift and the lensing potentials are nearly linear and Gaussian [91],[92]. Results reported in Hagstotz *et al.* 2015 [93] show that there are large effects on the CMB lensing power spectrum on scales well below $\ell \approx 1000$ (with contributions comparable to the power generated by nonlinear structure formation on small scales). The

majority of research in fact report that the effect on the CMB lensing convergence is indeed small, at least for current and near-future observations (see e.g. [91], [92], [94], [95]). More specifically, second- and higher-order corrections in the gravitational potential to the galaxy and CMB convergence are expected to give small corrections to the spherical harmonic power spectrum, which are at least two orders of magnitude lower than the leading order expansion on scales $\ell = 10^2$ to 10^4 (see e.g. [90],[94],[96],[97],[98]). For example, Pratten & Lewis 2016 [91] show that post-Born corrections make $\lesssim 0.2\%$ contribution to the CMB convergence power spectrum up to $\ell \lesssim 3000$, being well below cosmic variance.

However, recent work showed that post-Born corrections might become relevant when considering cross-correlations, for example between galaxy counts and CMB lensing [99],[100].

We conclude that invoking a fully ray-traced lightcone involving higher-order corrections becomes relevant when considering higher-order statistics of the convergence, smaller angular scales or considering cross-correlations between CMB lensing and other probes. Concerning the auto-power spectra, we expect the Born-induced errors on the power spectra to be well below 1% for the scales $\ell = 10^2$ to 10^4 [101].

Baryonic effects. Feedback processes from baryons are expected to have a significant impact on the weak lensing power spectrum [102],[103],[104]. Depending on the baryonic model considered, the effects on the weak lensing power spectrum can be up to 10% at $\ell \sim 10^3$. The present work is based on DM-only simulations, although the incorporation of baryonic effects, e.g. by using the *baryonic correction model* introduced in Schneider *et al.* [103] to mimic baryonic effects on the DM-only density field, remains an important extension of our pipeline and left for future work.

3.4 Codebase

We publish the UFALCON¹⁴ code, which contains the weak gravitational lensing part of the pipeline. The package is written in Python 3 and is publicly available on the Python Package index PYPI. The package documentation and some example-functions showing the user how to implement UFALCON are given in the repository.

The features of the released code include the fast computation of full-sky maps containing particle counts (particle-shells) from lightcone output and the subsequent fast construction of convergence maps for user-specific source galaxy redshift distributions and single-source redshifts. The released version of UFALCON currently supports the post-processing of N -Body simulation output in lightcone mode generated using the codes PKDGRAV3¹⁵ (Stadel *et al.* [46]) and L-PICOLA¹⁶ (Howlett *et al.* [36]).

4 Statistical Analysis

In this section, we perform several quantitative analyses on the full-sky maps of the different cosmological probes we obtained by applying our pipeline UFALCON on PKDGRAV3 simulation output, as described in section 3. All the maps are constructed for a redshift range between $z = 0.0$ and 1.75 and every set of γ_1 , δ_g , κ_{CMB} and ΔT_{ISW} maps are based on the same simulation output. We test the consistency of our simulation results by comparing to analytical predictions.

¹⁴UFALCON: <https://cosmology.ethz.ch/research/software-lab/UFalcon.html>

¹⁵<https://bitbucket.org/dpotter/pkdgrav3/>

¹⁶<https://cullanhowlett.github.io/l-picola/>

4.1 1-Point Distribution

We investigate the probability density function (PDF) of each map with $n_{\text{side}} = 1024$ by calculating the histogram as a function of pixel values. Figure 5 shows a comparison of the PDF's of the different probes obtained with UFALCON from PKDGRAV3 simulations with the PDF's generated from synthetic Gaussian maps by applying the HEALPIX subroutine `synfast` on analytical spherical harmonic power spectra computed with PYCOSMO. The distributions based on N -Body simulation output clearly deviates from a purely Gaussian field, which is also quantified by the skewness $S_3 = \mu_3/\sigma^3$ and the excess kurtosis $S_4 = \mu_4/\sigma^4 - 3$ of the non-Gaussian maps shown in each panel. The third and fourth central moment of the distributions are given by μ_3 and μ_4 respectively. Note that a Gaussian distribution has a skewness and an excess kurtosis of zero.

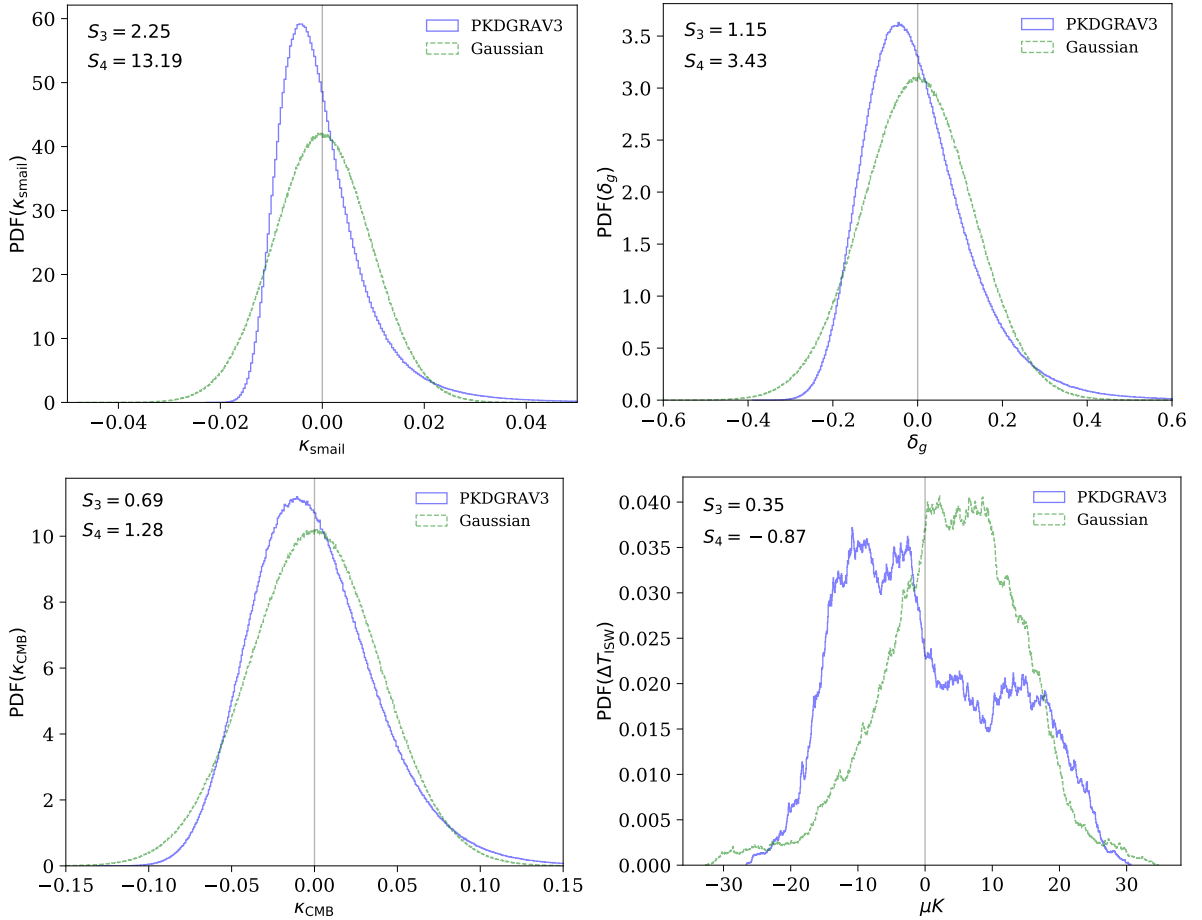


Figure 5: PDFs of the four different cosmological probes considered with a map resolution of $n_{\text{side}} = 1024$. The blue solid lines show the non-Gaussian results by applying our pipeline to UFALCON / PKDGRAV3 output and the green dashed lines show the distributions of Gaussian fields. The values for the skewness S_3 and excess kurtosis S_4 for the non-Gaussian distributions are shown in each panel.

4.2 Spherical Harmonic Power Spectrum

In this section, we present a comparison between our simulation results and analytical predictions for the spherical harmonic power spectra. Figure 6 shows the average power spectra of 630 sets of full-sky maps containing weak lensing shear, galaxy clustering, CMB lensing and temperature anisotropies from the ISW effect. The full-sky maps have been computed as described in section 3 and have a resolution of $n_{\text{side}} = 1024$. We first used the HEALPIX subroutine `anafast` to compute the auto- and cross- power spectra between the maps and then subtracted the corresponding shot noise contribution based on the Limber approximation given by equation (3.15). Furthermore, we adopt the correct deconvolution rules for the HEALPIX pixel window function and use a linear binning of $\delta\ell = 12$ to plot the power spectra. The blue solid lines show the simulation results and the black solid lines represent the analytical predictions computed with PYCOSMO based on a Limber approximation as described in section 2. The auto-power spectra of the different probes are shown on the diagonal and the cross-power spectra on the off-diagonal panels of the triangle plot. In Figure 7, we show the ratio between the analytical prediction and our simulation results for the spherical harmonic power spectrum. All the auto- and cross power spectra between the probes γ , δ_g and κ_{CMB} agree within 2% to the PYCOSMO prediction up to a multipole of $\ell \sim 1500$. The auto- and cross-power spectra including the temperature anisotropies from the ISW effect ΔT_{ISW} agree within 5% to the PYCOSMO prediction within the range from $\ell = 10^2$ to 10^3 with the exception of the cross-power spectrum $\langle \Delta T_{\text{ISW}} \gamma_1 \rangle$, which has a lower agreement. In general, we attribute the lower agreement of the cross-power spectrum between ΔT_{ISW} and the other probes to the potentially insufficient resolution of our ΔT_{ISW} maps for redshifts $z \lesssim 0.28$. As discussed in section 3.3.1, redshift $z \sim 0.28$ corresponds to the radial comoving distance where the linear size of the grid cells (for our choice of 1024^3 grid cells in the cubic grid used for the mass assignment scheme) corresponds to the pixel size of our HEALPIX maps when using $n_{\text{side}} = 1024$. The weak lensing shear window function W^γ peaks at around $z \sim 0.3$ for a Smail *et al.* distribution (shown in the right panel of Figure 10), whereas the weights of the other probes we consider peak at higher redshifts. The cross-correlation between ΔT_{ISW} and γ_1 is thus weighting the integrand more strongly for lower redshifts (which is also where the ISW-maps are potentially lacking resolution) and therefore has lower agreement to the theoretical predictions than the other cross-power spectra.

Our simulation results are lacking power on very large scales, i.e. on multipoles $\ell \lesssim 10$, which we attribute to missing large scale modes larger than our simulation volume (super sample covariance effects, see section 3.3.2 for a discussion thereof) and the inaccuracy of the Limber approximation for multipoles $\ell \lesssim 10$. This effect is not visible on the plots due to our choice of binning. Applying our randomization procedure to increase the number of realizations additionally enhances the power loss by 1-2 % on very large scales (see section 3.3.4). Note that since the present analysis is only considering scales between multipoles $\ell = 10^2$ and 10^3 , the observed missing power on multipoles $\ell \lesssim 10$ does not negatively affect the power spectrum covariance matrix.

4.3 Multi-Probe Covariance Matrix

We compute the joint covariance matrix from the $N_s = 630$ UFALCON full-sky realizations of the spherical harmonic power spectra $\hat{C}^{ij}(\ell)$ discussed in section 4.2 using the sample

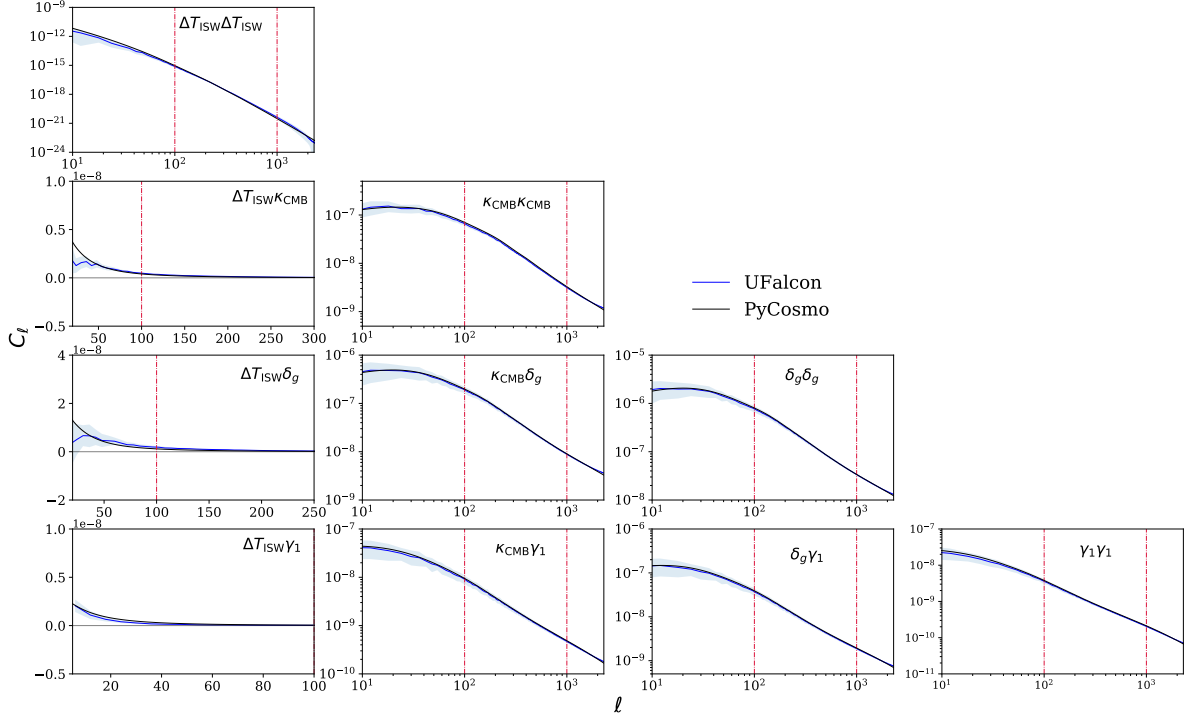


Figure 6: Blue solid lines: Mean auto- and cross- power spectra from 630 sets of full-sky maps for ΔT_{ISW} , κ_{CMB} , δ_g and γ_1 based on UFALCON / PKDGRAV3 output. The shaded blue area represent the standard deviation from 630 realizations. The vertical dot-dashed red lines indicate the angular scales of our interest $\ell = 10^2$ and $\ell = 10^3$. Black solid lines: Analytical predictions calculated with PYCOSMO based on the Limber approximation and using the fitting function from Mead *et al.* [54],[55].

covariance estimator

$$\hat{\Sigma}_{\ell, \ell'} = \frac{1}{N_s - 1} \sum_{k=1}^{N_s} \left[\hat{C}_k^{ij}(\ell) - \bar{C}_k^{ij}(\ell) \right] \left[\hat{C}_k^{i'j'}(\ell') - \bar{C}_k^{i'j'}(\ell') \right], \quad (4.1)$$

where $i, j, i', j' \in \{T_{\text{ISW}}, \kappa_{\text{CMB}}, \delta_g, \gamma_1\}$ denote the different cosmological probes and $\bar{C}_k^{ij}(\ell)$ is the mean over all realizations. For the case of Gaussian distributed data, the probability distribution of the sample covariance matrix is described by a Wishart distribution [105]. The variance of the sample covariance is then given by [106],[107]

$$\sigma^2(\hat{\Sigma}_{\ell, \ell'}) = \frac{1}{N_s - 1} \left(\Sigma_{\ell, \ell'}^2 + \Sigma_{\ell, \ell} \Sigma_{\ell', \ell'} \right). \quad (4.2)$$

In Figure 8 we show the diagonal components of the full-sky auto-power spectrum covariances divided by their corresponding Gaussian variances, denoted by $\hat{\Sigma}_{\ell, \ell'} / C_\ell^2 \cdot (N_\ell / 2)$. The number of modes between ℓ and $\ell + \Delta\ell$ is given by $N_\ell = A_s \Omega_s / (2\pi)^2$ with $A_s = 2\pi\ell\Delta\ell$ being the area of the 2D shell around the bin labelled with ℓ . The deviations from unity arise from the non-Gaussian error contribution present in our simulation results. Note that we obtain different results for the binned non-Gaussian covariance matrix, depending whether we first calculate the covariance with unit bin ($\delta\ell = 1$) and then manually re-bin it or when we directly calculate

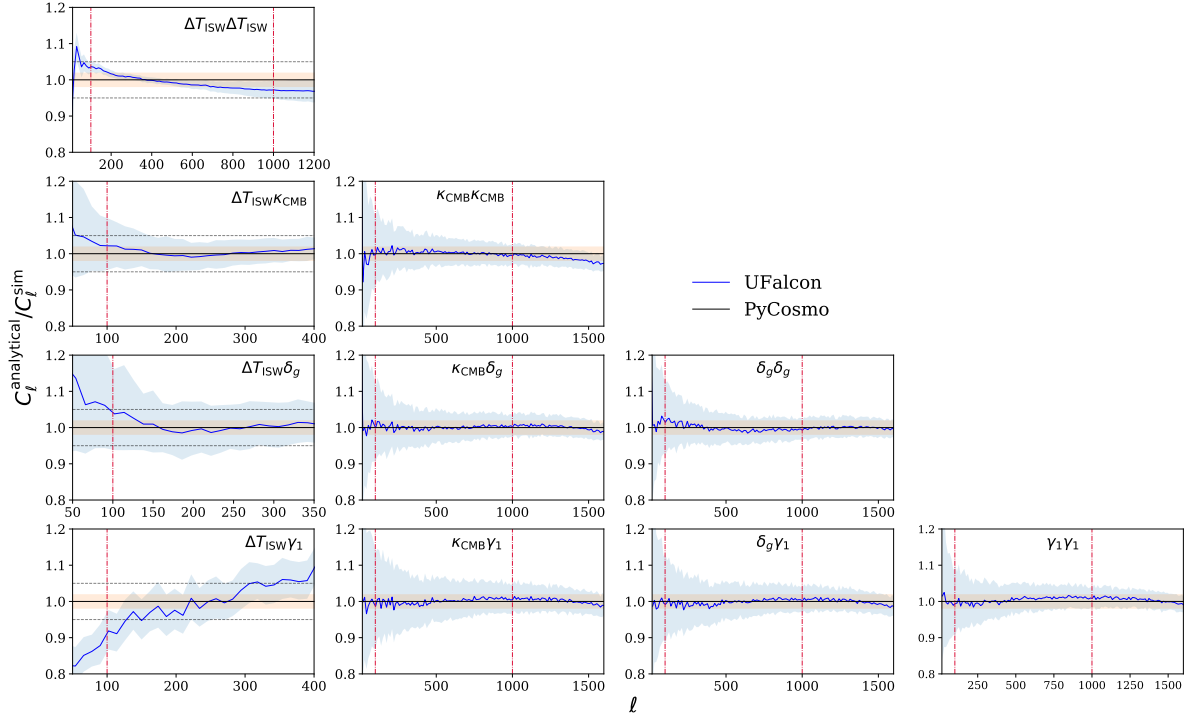


Figure 7: Ratio between analytical predictions based on PYCOSMO and the mean auto- and cross- power spectra from 630 sets of full-sky maps for ΔT_{ISW} , κ_{CMB} , δ_g and γ_1 based on UFALCON / PKDGRAV3 output. The shaded blue area represent the standard deviation from 630 realizations. The shaded orange area and the dashed grey lines represent 2% and 5% deviation from the analytical predictions respectively. The vertical dot-dashed red lines indicate the angular scales of our interest $\ell = 10^2$ and $\ell = 10^3$.

it at the bin-centers using broader ℓ -bins. Although for the case of a strongly off-diagonal covariance matrix we expect the difference to be small.

In the case of working with full-sky maps, only the presence of non-Gaussian contributions introduce off-diagonal components to the power spectrum covariance matrix. The relative strength of the off-diagonal terms to the diagonal terms in the covariance matrix can be quantified through the correlation coefficient as

$$\text{Corr}(\ell, \ell') = \frac{\hat{\Sigma}_{\ell, \ell'}}{\sqrt{\hat{\Sigma}_{\ell, \ell} \hat{\Sigma}_{\ell', \ell'}}}, \quad (4.3)$$

which is unity for $\ell = \ell'$. The correlation coefficient implies strong correlation for $\text{Corr} \rightarrow 1$, no correlation for $\text{Corr} \rightarrow 0$ or strong anti-correlation for $\text{Corr} \rightarrow -1$ between the spectra at different multipoles. In Figure 9, we show the joint covariance correlation matrix by using 630 sets of auto- and cross- spherical harmonic power spectra based on full-sky PKDGRAV3 simulations, whereas each spectrum spans a multipole range $\Delta\ell = [10^2, 10^3]$ with a linear binning of $\delta\ell = 100$. We additionally compute an analogous covariance matrix using equation (4.1) based on 630 sets of synthetic Gaussian maps. To this end, we follow the approach outlined in Giannantonio *et al.* [108] and applied in Nicola *et al.* [11], [12] in order to generate a set of correlated Gaussian maps. This approach consists of first generating correlated

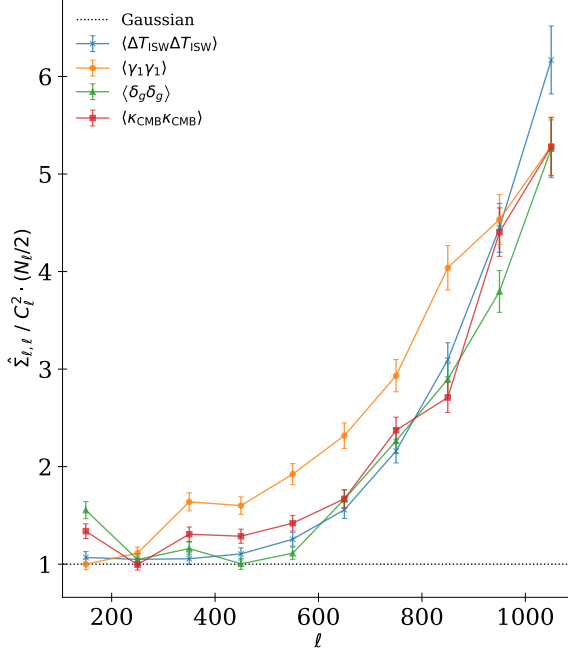


Figure 8: Diagonal components of the auto-power spectrum covariances for the simulated fields ΔT_{ISW} , γ_1 , δ_g and κ_{CMB} divided by the Gaussian covariances given by $\hat{\Sigma}_{\ell,\ell}/C_\ell^2 \cdot (N_\ell/2)$. The errorbars correspond to the standard deviation obtained by using equation (4.2) and assuming that our covariance matrix estimate follow a Wishart distribution.

realizations of the spin-0 fields ΔT_{ISW} , κ_{CMB} , δ_g and κ_{smail} . The obtained convergence map κ_{smail} based on the redshift distribution given by equation (3.5) is then transformed to the spin-2 weak lensing shear fields γ_1 and γ_2 using equation (3.6). Further details about our implementation of this algorithm are given in Appendix C.

5 Forecast

In this section we compute constraints on cosmological parameters in order to quantify the impact of the non-Gaussian contributions to the covariance matrix and of the combination of different auto- and cross-power spectra.

Survey specifications. This analysis is performed for a stage IV-like survey area, i.e. we mask half of the sky (including masking a simplified galactic annulus) leading to a map geometry with an unmasked sky fraction of $f_{\text{sky}} \sim 0.42$, as shown in the left panel of Figure 10. The same survey mask is then applied to each map of the cosmological probes γ , δ_g , κ_{CMB} and ΔT_{ISW} for all the 630 sets of full-sky UFALCON maps. Each map covers a redshift range between $z = 0.0$ and 1.75 . Furthermore, the cosmic shear γ and galaxy clustering δ_g maps are generated using a Smail *et al.* [83] source galaxy distribution (given by equation (3.5) and shown in the right panel of Figure 10). We intentionally do not add survey-related noise to our simulated maps (such as shape noise for cosmic shear), which would increase the diagonal components of our covariance matrices and therefore potentially degrade the relative impact

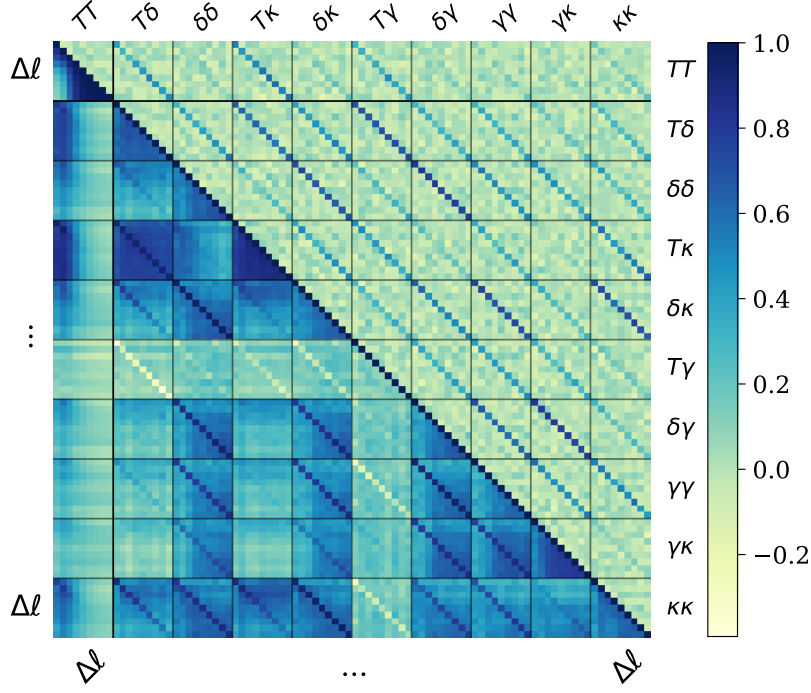


Figure 9: Multi-probe covariance correlation matrix for the spherical harmonic power spectra derived using 630 full-sky realizations. Each panel covers the multipole range $\Delta\ell = [10^2, 10^3]$ with a linear binning of $\delta\ell = 100$. Lower triangle: Non-Gaussian correlation matrix obtained by applying UFALCON to PKDGRAV3 simulations. Upper triangle: Correlation matrix based on synthetic Gaussian realizations.

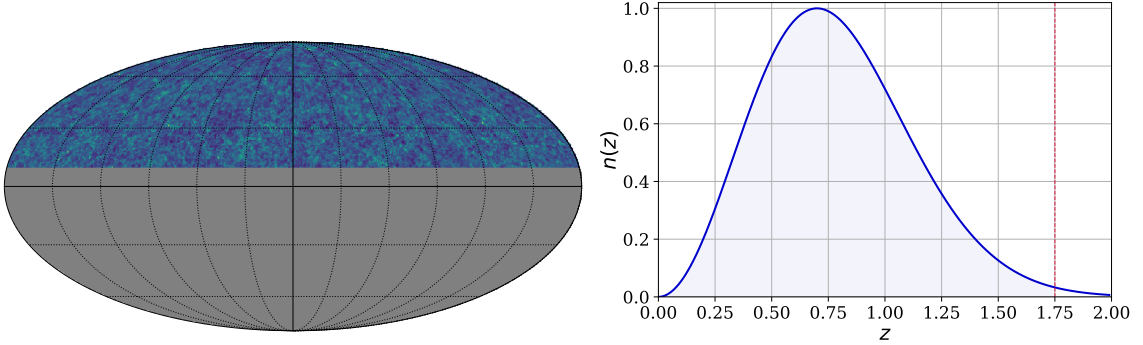


Figure 10: Left panel: Stage-IV-like survey area covering $\sim 17000 \text{ deg}^2$. Right panel: Smail *et al.* [83] source galaxy redshift distribution given by equation (3.5) used to generate the γ and δ_g maps. The vertical dashed red line at $z_{\text{max}} = 1.75$ indicates the upper redshift bound, up to which our analysis has been performed.

of the non-Gaussian error contribution to the covariance. Our forecast analysis is therefore only limited by cosmic variance.

In order to parametrise the observational and sky systematics involved in the cosmological measurements, we introduce four different multiplicative bias parameters m_i for the estimator \hat{i} of each probe as

$$\hat{i} = (1 + m_i)i, \quad (5.1)$$

where $i \in \{T_{\text{ISW}}, \kappa_{\text{CMB}}, \delta_g, \gamma_1\}$. Motivated by the cosmological analysis done in Nicola *et al.* [11], [12], the introduction of scalar multiplicative bias parameters for the weak lensing shear can take into account calibration uncertainties [109] and uncertainties in the amplitude due to intrinsic alignment of unlensed galaxies (see Appendix A in [12]). Furthermore, a multiplicative bias parameter can be introduced to take into account the normalisation uncertainty of the CMB lensing convergence estimator [12]. We additionally introduce nuisance parameters for the CMB temperature anisotropies due to the ISW effect ΔT_{ISW} and the galaxy overdensity δ_g , which can parametrise possible foreground contamination. Concerning the latter, we set the linear galaxy bias parameter to $b = 1$. The introduced nuisance parameters m_i are simultaneously fit with the cosmological parameters θ . Note that our analysis does not include other systematic effects, such as baryonic effects on the power spectrum or photometric redshifts uncertainties. Moreover, the present work represents a non-tomographic analysis.

Pseudo- C_ℓ estimation. For our analysis we rely on the application of the pseudo- C_ℓ method, which was first proposed in [110] and [111], and is based on the original method in [112]. Extending this framework to spin-0 and spin-2 fields, we relate the underlying full-sky analytical predictions based on PYCOSMO to the observed cut-sky power spectra \tilde{C}_ℓ through

$$\tilde{C}_\ell = \sum_{\ell'} \mathbf{M}_{\ell\ell'} \mathbf{C}_{\ell'}^{\text{PyCosmo}}, \quad (5.2)$$

where \mathbf{M} denotes the mode-coupling matrix describing the effect of the sky-cut applied to the data. A more detailed explanation of our implementation of this method is given in appendix D.

Parameter inference. We assume a joint likelihood given by [113], [114]

$$\mathcal{L}(D|\theta, \hat{\Sigma}, N_s) \propto |\hat{\Sigma}|^{-1/2} \left[1 + \frac{(\mathbf{C}_\ell^{\text{obs}} - \tilde{\mathbf{C}}_\ell)^T \hat{\Sigma}^{-1} (\mathbf{C}_\ell^{\text{obs}} - \tilde{\mathbf{C}}_\ell)}{N_s - 1} \right]^{-\frac{N_s}{2}}, \quad (5.3)$$

which takes into account the uncertainty of the covariance matrix estimated from simulations. The covariance matrix is estimated using equation (4.1) for 630 masked realizations based on simulations and based on synthetic Gaussian maps as described in section 4.3. We approximate the covariance matrices to be cosmology independent, i.e. they are based on simulation and Gaussian realizations for fixed fiducial parameters values θ_{fid} . The calculation of a cosmology dependent covariance matrix would require running the same number of simulations for various cosmological parameters combinations and is therefore computationally very expensive.

The 'mock observation' power spectrum vector is set to $\mathbf{C}_\ell^{\text{obs}} = \tilde{\mathbf{C}}_\ell(\theta_{\text{fid}})$, i.e. to the pseudo- C_ℓ vector based on the analytical prediction computed with PYCOSMO for our fiducial parameters θ_{fid} . This choice of data vector allows us to isolate the effect of using different covariance matrices for the parameter inference. The resulting constraints are therefore expected to be centered around the fiducial cosmology and not experience any change in area

/ position due to added noise on the data vector. The analytical prediction is computed as $\mathbf{C}_\ell^{\text{th}} = \tilde{\mathbf{C}}_\ell(\boldsymbol{\theta})$ for varying parameters $\boldsymbol{\theta}$ and has the same dimensionality as $\mathbf{C}_\ell^{\text{obs}}$. The total power spectrum vector with dimensionality d has the form

$$\mathbf{C}_\ell = \begin{pmatrix} C_\ell^{TT} & C_\ell^{T\delta} & C_\ell^{\delta\delta} & C_\ell^{\kappa T} & C_\ell^{\kappa\delta} & C_\ell^{T\gamma} & C_\ell^{\gamma\delta} & C_\ell^{\kappa\gamma} & C_\ell^{\gamma\gamma} & C_\ell^{\kappa\kappa} \end{pmatrix}, \quad (5.4)$$

where $T = \Delta T_{\text{ISW}}$, $\delta = \delta_g$, $\kappa = \kappa_{\text{CMB}}$ and $\gamma = \gamma_1$ for notational brevity. Furthermore, the power spectrum vectors and the covariance matrices are binned linearly with $\delta\ell = 100$ within a multipole range $\Delta\ell = [10^2, 10^3]$. Note that since we examine the effect of combining different auto- and cross-power spectra, the combination of power spectra and the dimensionality d in the covariance matrix and the above vectors depend on the considered probes.

We sample the joint likelihood given by equation (5.3) in a Monte Carlo Markov Chain (MCMC) to obtain cosmological parameters constraints using UHAMMER¹⁷, which is based on the EMCEE sampler [115]. Therefore we vary 5 cosmological parameters $\{h, \Omega_m, \Omega_b, n_s, \sigma_8\}$ and up to 4 nuisance parameters $\{m_{\Delta T_{\text{ISW}}}, m_{\kappa_{\text{CMB}}}, m_{\delta_g}, m_{\gamma_1}\}$, depending on the probes considered for the analysis. We assume flat priors for all the parameters with width $h \in [0.2, 1.2]$, $\Omega_m \in [0.1, 0.7]$, $\Omega_b \in [0.01, 0.09]$, $n_s \in [0.1, 1.8]$, $\sigma_8 \in [0.4, 1.5]$ and $m_i \in [-0.2, 0.2]$. Note that we do not observe any change in the resulting parameter constraints for any combination of probes when increasing the (flat) prior range for the nuisance parameters m_i beyond $[-0.15, 0.15]$. Our choice of flat priors $m_i \in [-0.2, 0.2]$ is therefore not compromising our results and leading to a faster convergence of our MCMC runs compared to when using broader priors.

Cosmological constraints. Figure 11 shows parameter constraints for Ω_m and σ_8 (the associated 68% and 95% confidence limits) by using the auto-power spectra of the different probes separately and the corresponding simulation-based non-Gaussian covariance matrices. The combination of the different probes potentially allows us to break the degeneracy between Ω_m and σ_8 . As can be seen from the figure, the contours computed from the ΔT_{ISW} auto-power spectrum are broader than the ones obtained from the other auto-power spectra. The ISW effect leads to secondary CMB anisotropies on linear scales, which affects the CMB temperature power spectrum on large scales. On such scales, the primordial anisotropies and cosmic variance dominate the signal and therefore complicate a direct detection of the ISW signal in the full CMB temperature field. In order to detect the ISW signal, one can consider the cross-correlation of the CMB temperature fluctuations with other tracers of the gravitational potential [68]. Thus, the inclusion of the ΔT_{ISW} auto-power spectrum in our analysis remains somewhat theoretical.

In Figure 12, we show the constraints in the $\Omega_m - \sigma_8$ plane when adopting a Gaussian covariance matrix (green contours) and a non-Gaussian covariance matrix measured from simulations (blue contours). As seen in all four panels for each individual probe, the effect of the non-Gaussian error contribution in the covariance matrix (in the absence of added noise, such as shape noise for weak lensing shear) is crucial for an accurate inference of cosmological parameters. The impact of non-Gaussian components in the covariance matrix in general increase the size of the obtained parameters constraints, as previously observed in Sato *et al.* [17] for the weak lensing power spectrum. More quantitatively and concerning our results, the

¹⁷<http://cosmo-docs.phys.ethz.ch/uhammer/>

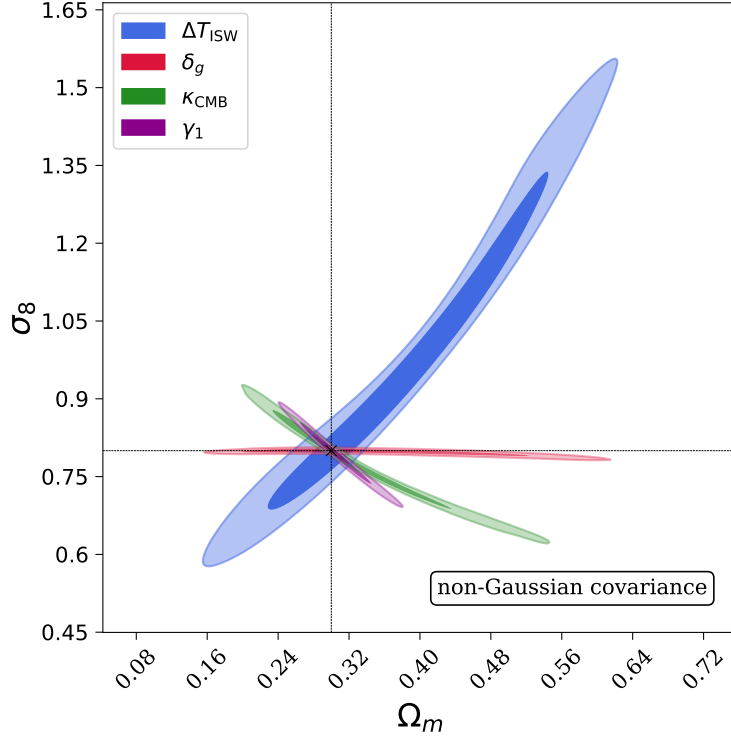


Figure 11: Parameter constraints for Ω_m and σ_8 derived from separate single-probe analyses based on the auto-power spectrum using a simulation-based non-Gaussian covariance matrix. The constraints are marginalized over the nuisance parameters. The inner (outer) contours depict the 68% (95%) confidence levels. Note that our forecast analysis is only limited by cosmic variance, i.e. no survey-specific noise has been added to our simulated maps.

95% confidence levels for the parameters Ω_m and σ_8 increase by $\sim 10\%$, $\sim 20\%$, $\sim 20\%$ and $\sim 40\%$ for the probes ΔT_{ISW} , κ_{CMB} , δ_g , γ_1 respectively when changing from using a Gaussian to using a non-Gaussian covariance matrix.

We further study the impact of different probe-combinations on the cosmological parameter constraints in the context of adopting a Gaussian or non-Gaussian covariance matrix. In Figure 13, we show the integrated parameter constraints obtained when performing a joint fit of the auto-power spectra $\mathbf{C}_\ell = (C_\ell^{TT}, C_\ell^{\delta\delta}, C_\ell^{\gamma\gamma}, C_\ell^{\kappa\kappa})$ with total dimension $d = 36$ (each power spectrum has 9 multipole bins, i.e. dimension $d = 9$) and jointly fitting all auto- and cross-power spectra of total dimension $d = 90$ (given by equation (5.4)), for a Gaussian and non-Gaussian covariance matrix respectively. The parameter contours displaying the 4 varied nuisance parameters are shown in Appendix F.

For both choices of covariance matrices the inclusion of the cross-correlations increases the information gain in the parameter constraints significantly. This effect is enhanced through our use of additional nuisance parameters for each probe. As one can clearly see from Figure 13, adopting a non-Gaussian covariance matrix increases the size of the inferred constraints compared to when using a Gaussian approximation. We observe this effect when fitting only the auto-power spectra (shown in the left panel of Figure 14) and also when including the cross-power spectra in the analysis (shown in the right panel of Figure 14). This behavior is expected, as the non-Gaussian contributions introduce non-diagonal elements in

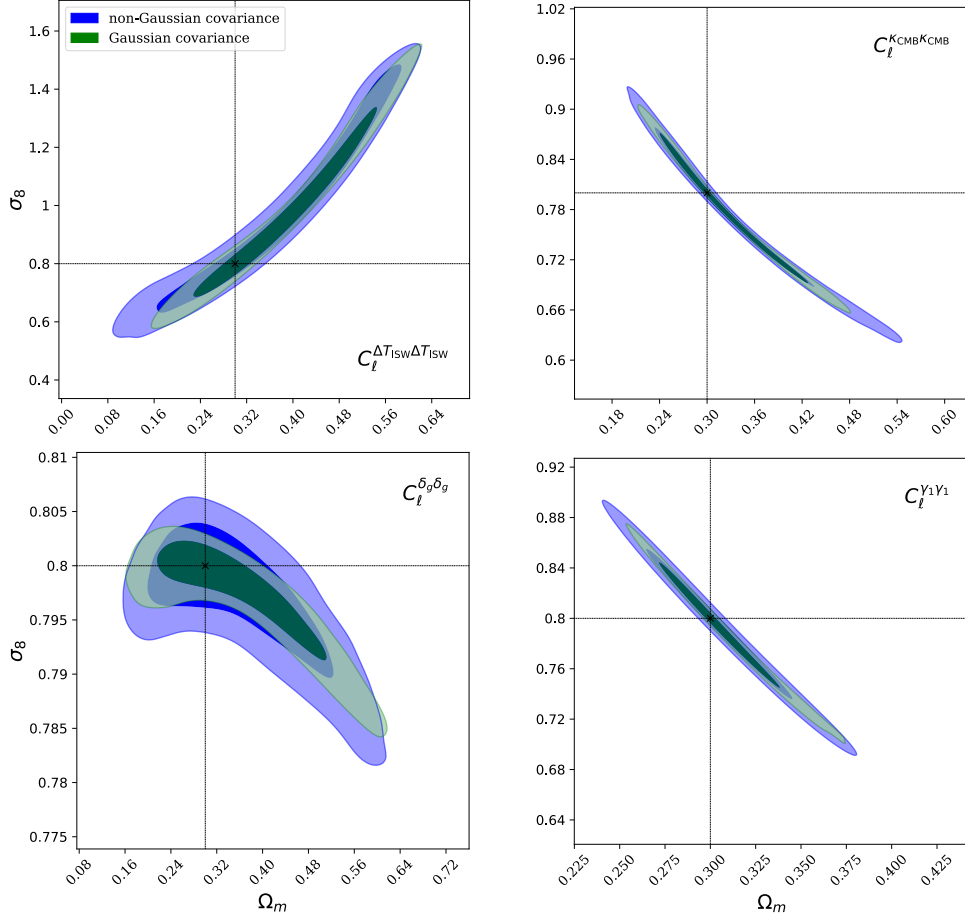


Figure 12: Cosmological parameter constraints for Ω_m and σ_8 derived from a single-probe analysis based on the auto-power spectra using a Gaussian (green contours) and simulation-based non-Gaussian (blue contours) covariance matrix. The inner (outer) contours depict the 68% (95%) confidence levels. Note that our forecast analysis is only limited by cosmic variance, i.e. no survey-specific noise has been added to our simulated maps.

the covariance matrix, which in turn lead to broader constraints in general.

In order to investigate our results for the different setup configurations, we compute the change in area of the 95% confidence levels between using a Gaussian and using a simulation-based non-Gaussian covariance matrix. Figure 15 shows the change in area averaged over all cosmological parameter combinations for different probe-combinations. In general, we observe that the impact of the non-Gaussian error contribution to the covariance matrix becomes increasingly important as further cosmological probes are incorporated in the analysis. Invoking only the auto-power spectra, we observe that the mean area of our obtained contours increase by a factor of ~ 3 . When we further include the cross-power spectra, the impact of the non-Gaussian covariance matrix on the size of the contours is smaller: The additional constraining power coming from the cross-correlations between the probes counteracts the effect of adding non-Gaussian corrections to the covariance matrix to some degree. We expect this effect to be enhanced by our use of nuisance parameters. Considering the $\Omega_m - \sigma_8$ plane, we observe a increase by a factor of ~ 3.4 and ~ 2.5 when using only the auto-power spectra and the

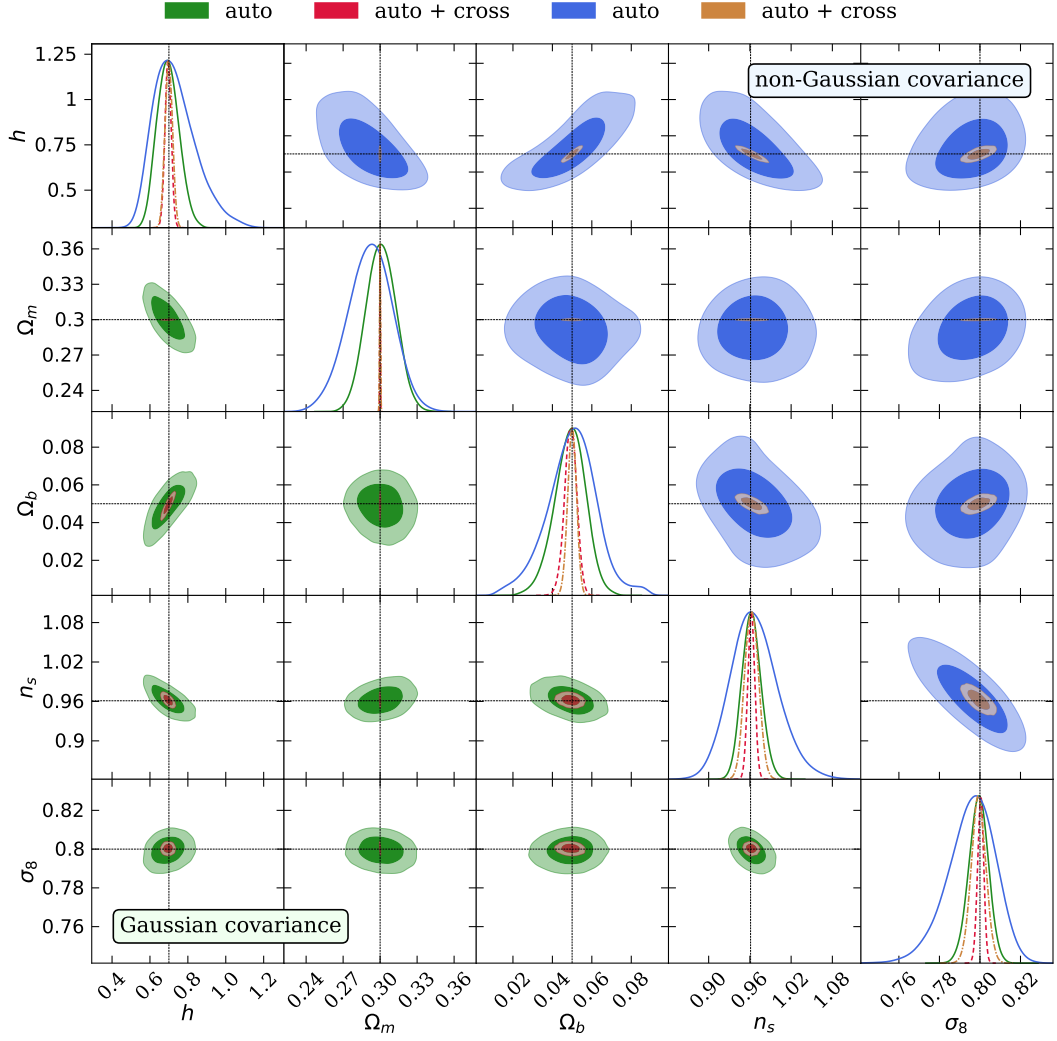


Figure 13: Parameter constraints for the parameters described in section 5 marginalized over the nuisance parameters. The lower (upper) triangle-plot show the contours obtained when using a Gaussian (non-Gaussian) covariance matrix. The green (blue) and red (brown) contours in the lower (upper) triangle-plot are obtained using only the auto-power spectra and the auto- and cross-power spectra respectively. The inner (outer) contours depict the 68% (95%) confidence levels. Note that our forecast analysis is only limited by cosmic variance, i.e. no survey-specific noise has been added to our simulated maps.

auto- and cross-power spectra respectively.

6 Conclusion

In the present work, we have added to our UFALCON package the functionality to generate a *set* of full-sky maps for different cosmological probes in a self-consistent way based on the same underlying simulated matter density field with a minimal runtime of ~ 1 walltime-hour. This set contains full-sky maps of different cosmological probes for a redshift range between

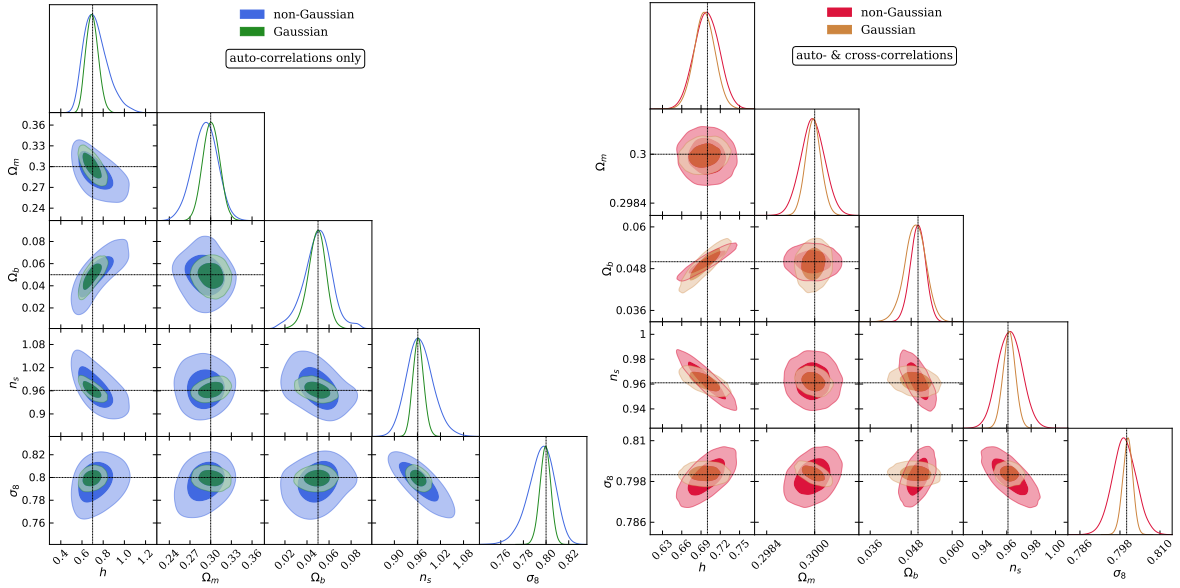


Figure 14: Parameter constraints for the parameters described in section 5 marginalized over the nuisance parameters (same constraints as in Figure 13, but shown in a different combination). Left panel: The blue (green) constraints are obtained by using only the auto-power spectra with the corresponding non-Gaussian (Gaussian) covariance matrix. Right panel: The red (brown) constraints are obtained by using the auto- and cross-power spectra with the corresponding non-Gaussian (Gaussian) covariance matrix. The inner (outer) contours depict the 68% (95%) confidence levels. Note that our forecast analysis is only limited by cosmic variance, i.e. no survey-specific noise has been added to our simulated maps.

$z = 0.0$ and 1.75 such as weak lensing shear, galaxy clustering including RSD, CMB lensing and CMB temperature anisotropies from the ISW effect.

The past-lightcone is thereby constructed by first replicating the simulation volume 6 times along each axis and then performing a weighted projection of the DM particles onto the sphere for cosmic shear, galaxy clustering and CMB convergence. In order to obtain continuous full-sky maps of the ISW induced temperature fluctuations and CMB lensing potential maps, the 3D-matter density field is interpolated and evaluated along each line of sight. The replication procedure allows us to cover a large enough survey volume with a sufficiently high resolution. We increase the number of quasi-independent realizations obtained from one N -Body simulation by applying random transformations to the periodically arranged density fields. A version of the UFALCON package containing the weak gravitational lensing part of the pipeline is publicly available and a short description is given in section 3.4.

We then computed various statistical quantities, such as the auto- and cross- spherical harmonic power spectra between the different simulated full-sky maps. We find better than 2% agreement between the analytical predictions and our simulation-based auto- and cross-power spectrum results in the multipole range $\ell = 10^2$ to 10^3 for the probes γ , δ_g and κ_{CMB} . Our results agree within $\sim 5\%$ to the analytical predictions in the same multipole range when considering auto- and cross-correlations including ΔT_{ISW} , with the exception of the cross-power spectrum $C_\ell^{\Delta T_{\text{ISW}}\gamma}$, which shows a lower agreement. From an ensemble of 630 simulated realizations, we have estimated a multi-probe covariance matrix for the multipole

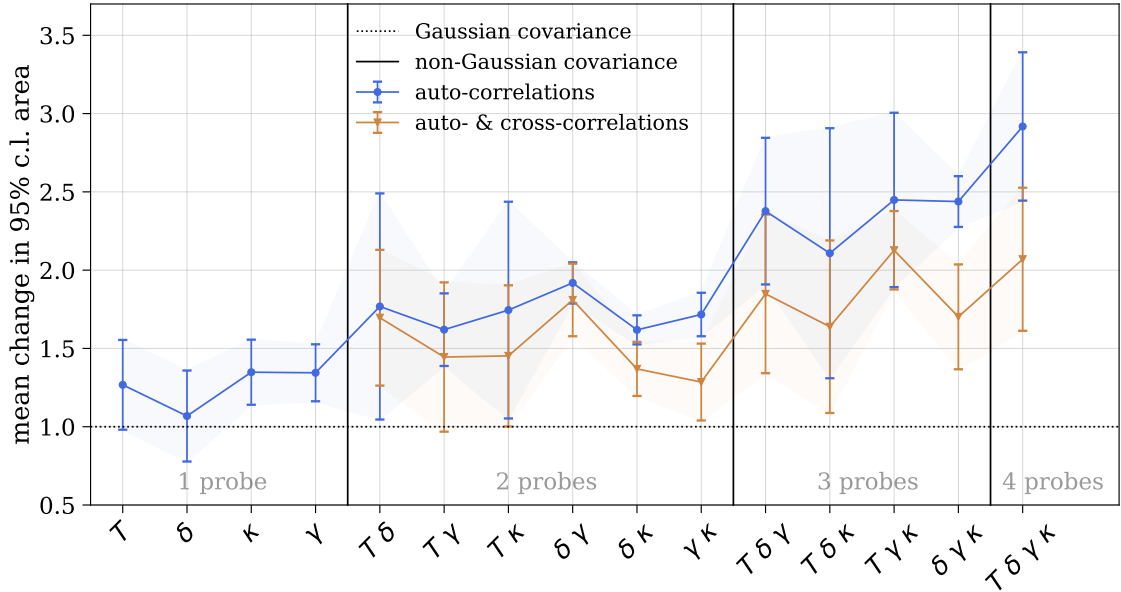


Figure 15: The blue (brown) lines represent the mean change in 95% confidence level area from using a Gaussian (dotted line) to using a non-Gaussian covariance matrix (solid lines). The error bars represent the 1σ -error on the change in 95% confidence level area for the 10 two-dimensional contours obtained for different combinations of cosmological parameters. Note that our forecast analysis is only limited by cosmic variance, i.e. no survey-specific noise has been added to our simulated maps.

range $\ell \in [10^2, 10^3]$.

We further have analysed the impact of the non-Gaussian covariance matrix based on simulations on cosmological parameter constraints by performing a joint likelihood analysis for a stage-IV-like survey geometry. Note that we have neglected any additional survey-specific noise-contribution to the covariance matrix in order to isolate the effect of the non-Gaussian term. We first studied the impact of using a non-Gaussian covariance matrix on the parameter constraints when performing separate inferences for each auto-power spectrum of the different probes. Here we observe an increase of $\sim 10\%$, $\sim 20\%$, $\sim 20\%$ and $\sim 40\%$ in the area of the 95% confidence level in the $\Omega_m - \sigma_8$ plane for the probes ΔT_{ISW} , κ_{CMB} , δ_g and γ respectively when using a non-Gaussian covariance matrix instead of a Gaussian approximation.

Furthermore, we studied the effect of different probe-combinations in a joint likelihood analysis using both a Gaussian and a simulation-based non-Gaussian multi-probe covariance matrix. We have therefore introduced a multiplicative bias parameter for each probe considered. From this analysis, we observe that the inclusion of the cross-correlation significantly increases the information gain. The importance of using a covariance matrix which includes non-Gaussian contributions compared to using a Gaussian approximation becomes even more apparent in the context of a multi-probe analysis: We observe a mean increase of the 95% confidence level area over all cosmological parameters by a factor of ~ 3 and ~ 2 when using only the auto-power spectra and when including auto- and cross-power spectra in the analysis respectively.

The combination of different probes of the large-scale structure of the Universe can lead to significant information gain in cosmological parameters. Further taking into account the cross-correlations between multiple probes based on different physical fields offer more stringent tests of the systematics and can potentially reveal new physics. This is crucial as future surveys become increasingly systematics limited. As combining multiple probes increases the size of the data vector and the retrievable information content, an accurate estimate of the covariance matrix is of uttermost importance. Although using a Gaussian approximation might be sufficient for some ongoing surveys, it will ultimately be crucial to take into account non-Gaussianity for future large surveys.

Acknowledgments

We thank Douglas Potter and Joachim Stadel from the University of Zürich for the distribution of the code PKDGRAV3 and for their continuous support with the code. We would also like to thank Björn Malte Schäfer and Aurel Schneider for very helpful discussions concerning the pipeline and Christiane Lorenz for careful reading of the manuscript. Furthermore, we thank Uwe Schmitt for his help with the computing implementation. AR is grateful for the hospitality of KIPAC at Stanford University/SLAC where part of his contribution was made. We acknowledge support by the Swiss National Science Foundation grant 200021_169130. AA is supported by a Royal Society Wolfson Fellowship. This research made use of IPython, NumPy, SciPy, Matplotlib, Healpy, PyCosmo, UHammer and GetDist.

References

- [1] R. Sgier, A. Refregier, A. Amara, and A. Nicola, “Fast generation of covariance matrices for weak lensing,” *JCAP*, vol. 2019, p. 044, January 2019.
- [2] M. Kilbinger, L. Fu, C. Heymans, F. Simpson, and J. B. et al., “Cfhtlens: combined probe cosmological model comparison using 2d weak gravitational lensing,” *MNRAS*, vol. 430, pp. 2200–2220, April 2013.
- [3] T. D. E. S. Collaboration, “Cosmology from cosmic shear with dark energy survey science verification data,” *Phys. Rev. D*, vol. 94, July 2016.
- [4] D. Weinberg, M. Mortonson, D. Eisenstein, C. Hirata, A. Riess, and E. Rozo, “Observational probes of cosmic acceleration,” *Elsevier*, vol. 530, pp. 87–255, September 2013.
- [5] R. Sunyaev and Y. B. Zel’dovich, “The observations of relic radiation as a test of the nature of x-ray radiation from the clusters of galaxies,” *Comments on Astrophysics and Space Physics*, vol. 4, p. 173, November 1972.
- [6] R. Bielby, T. Shanks, U. Sawangwit, S. M. Croom, N. P. Ross, and D. A. Wake, “Photometric selection of emission-line galaxies, clustering analysis and a search for the integrated sachs–wolfe effect,” *MNRAS*, vol. 403, pp. 1261–1273, April 2010.
- [7] A. Cooray, “Integrated sachs-wolfe effect: Large scale structure correlation,” *Phys. Rev. D*, vol. 65, p. 103510, April 2002.
- [8] P. Fosalba, E. Gaztañaga, , and F. J. Castander, “Detection of the integrated sachs-wolfe and sunyaev-zeldovich effects from the cosmic microwave background–galaxy correlation,” *ApJ*, vol. 597, pp. 89–92, November 2003.
- [9] R. Mandelbaum, A. Slosar, T. Baldauf, U. Seljak, C. Hirata, R. Nakajima, R. Reyes, and R. Smith, “Cosmological parameter constraints from galaxy–galaxy lensing and galaxy clustering with the sdss dr7,” *MNRAS*, vol. 432, pp. 1544–1575, April 2013.

- [10] M. Cacciato, F. van den Bosch, S. More, H. Mo, and X. Yang, “Cosmological constraints from a combination of galaxy clustering and lensing – iii. application to sdss data,” *MNRAS*, vol. 430, pp. 767–786, April 2013.
- [11] A. Nicola, A. Refregier, and A. Amara, “Integrated approach to cosmology: Combining cmb, large-scale structure, and weak lensing,” *Phys. Rev. D*, vol. 94, October 2016.
- [12] A. Nicola, A. Refregier, and A. Amara, “Integrated cosmological probes: Extended analysis,” *Phys. Rev. D*, vol. 95, April 2017.
- [13] A. Barreira, E. Krause, and F. Schmidt, “Accurate cosmic shear errors: do we need ensembles of simulations?,” *JCAP*, vol. 2018, October 2018.
- [14] E. Krause and T. Eifler, “cosmolike – cosmological likelihood analyses for photometric galaxy surveys,” *MNRAS*, vol. 470, pp. 2100–2112, September 2017.
- [15] S. Hilbert, J. Hartlap, and P. Schneider, “Cosmic shear covariance: the log-normal approximation,” *AA*, vol. 536, December 2011.
- [16] M. Sato, T. Hamana, R. Takahashi, M. Takada, N. Yoshida, T. Matsubara, and N. Sugiyama, “Simulations of wide-field weak lensing surveys i: Basic statistics and non-gaussian effects,” *ApJ*, vol. 701, July 2009.
- [17] M. Sato and T. Nishimichi, “Impact of the non-gaussian covariance of the weak lensing power spectrum and bispectrum on cosmological parameter estimation,” *Phys. Rev. D*, vol. 87, June 2013.
- [18] R. Scoccimarro, M. Zaldarriaga, and L. Hui, “Power spectrum correlations induced by nonlinear clustering,” *ApJ*, vol. 527, no. 1, 1999.
- [19] D. Bertolini, K. Schutz, M. Solon, and K. Zurek, “The trispectrum in the effective field theory of large scale structure,” *JCAP*, vol. 2016, June 2016.
- [20] D. Bertolini, K. Schutz, M. Solon, J. Walsh, and K. Zurek, “Non-gaussian covariance of the matter power spectrum in the effective field theory of large scale structure,” *Phys. Rev. D*, vol. 93, June 2016.
- [21] D. Bertolini and M. Solon, “Principal shapes and squeezed limits in the effective field theory of large scale structure,” *JCAP*, vol. 2016, November 2016.
- [22] A. Cooray and R. Sheth, “Halo models of large scale structure,” *Elsevier*, vol. 372, pp. 1–129, December 2002.
- [23] R. Takahashi, N. Yoshida, M. Takada, T. Matsubara, N. Sugiyama, I. Kayo, A. Nishizawa, T. Nishimichi, P. Saito, and A. Taruya, “Simulations of baryon acoustic oscillations ii: covariance matrix of the matter power spectrum,” *ApJ*, vol. 700, July 2009.
- [24] M. Sato, M. Takada, T. Hamana, and T. Matsubara, “Simulations of wide-field weak lensing surveys ii: Covariance matrix of real space correlation functions,” *ApJ*, vol. 734, May 2011.
- [25] J. Harnois-Deraps, S. Vafaei, and L. V. Waerbeke, “Gravitational lensing simulations – i. covariance matrices and halo catalogues,” *MNRAS*, vol. 426, pp. 1262–1279, October 2012.
- [26] L. Blot, P. Corasaniti, J.-M. Alimi, V. Reverdy, and Y. Rasera, “Matter power spectrum covariance matrix from the deus-pur lcdm simulations: mass resolution and non-gaussian errors,” *MNRAS*, vol. 446, pp. 1756–1764, November 2015.
- [27] R. Takahashi, T. Hamana, M. Shirasaki, T. Namikawa, T. Nishimichi, K. Osato, and K. Shiroyama, “Full-sky gravitational lensing simulation for large-area galaxy surveys and cosmic microwave background experiments,” *ApJ*, vol. 850, November 2017.
- [28] A. Petri, Z. Haiman, and M. May, “Sample variance in weak lensing: How many simulations are required?,” *Phys. Rev. D*, vol. 93, March 2016.

- [29] A. Klypin and F. Prada, “Dark matter statistics for large galaxy catalogues: power spectra and covariance matrices,” *MNRAS*, vol. 478, pp. 4602–4621, August 2018.
- [30] J. Harnois-Deraps, A. Amon, A. Choi, V. Demchenko, C. Heymans, A. Kannawadi, R. Nakajima, E. Sirks, L. V. Waerbeke, Y.-C. Cai, B. Giblin, H. Hildebrandt, H. Hoekstra, L. Miller, and T. Troester, “Cosmological simulations for combined-probe analyses: covariance and neighbour-exclusion bias,” *MNRAS*, vol. 481, pp. 1337–1367, November 2018.
- [31] O. Friedrich and T. Eifler, “Precision matrix expansion – efficient use of numerical simulations in estimating errors on cosmological parameters,” *MNRAS*, vol. 473, pp. 4150–4163, October 2017.
- [32] B. Joachimi, “Non-linear shrinkage estimation of large-scale structure covariance,” *MNRAS*, vol. 466, pp. L83–L87, November 2016.
- [33] S. Dodelson and M. D. Schneider, “The effect of covariance estimator error on cosmological parameter constraints,” *Phys. Rev. D*, vol. 88, September 2013.
- [34] S. Tashev, M. Zaldarriaga, and D. Eisenstein, “Solving large scale structure in ten easy steps with cola,” *JCAP*, vol. 2013, June 2013.
- [35] J. Koda, C. Blake, F. Beutler, E. Kazin, and F. Marin, “Fast and accurate mock catalogue generation for low-mass galaxies,” *MNRAS*, vol. 459, pp. 2118–2129, June 2016.
- [36] C. Howlett, M. Manera, and W. Percival, “L-picola: A parallel code for fast dark matter simulation,” *Astronomy and Computing*, vol. 12, pp. 109–126, September 2015.
- [37] H. Winther, K. Koyama, M. Manera, B. Wright, and G.-B. Zhao, “Cola with scale-dependent growth: applications to screened modified gravity models,” *JCAP*, vol. 2017, August 2017.
- [38] B. Wright, H. Winther, and K. Koyama, “Cola with massive neutrinos,” *JCAP*, vol. 2017, October 2017.
- [39] A. Izard, M. Crocce, and P. Fosalba, “Ice-cola: towards fast and accurate synthetic galaxy catalogues optimizing a quasi-n-body method,” *MNRAS*, vol. 459, pp. 2327–2341, July 2016.
- [40] A. Izard, P. Fosalba, and M. Crocce, “Ice-cola: fast simulations for weak lensing observables,” *MNRAS*, vol. 473, pp. 3051–3061, January 2017.
- [41] T. Kacprzak, J. Herbel, A. Nicola, R. Sgier, F. Tarsitano, C. Bruderer, A. Amara, and A. R. et al., “Monte carlo control loops for cosmic shear cosmology with des year 1.” arXiv:1906.01018, June 2019.
- [42] J. Fluri, T. Kacprzak, R. Sgier, A. Refregier, and A. Amara, “Weak lensing peak statistics in the era of large scale cosmological surveys,” *J. Cosmol. Astropart. Phys.*, vol. 2018, October 2018.
- [43] J. Fluri, T. Kacprzak, A. Refregier, A. Amara, A. Lucchi, and T. Hofmann, “Cosmological constraints from noisy convergence maps through deep learning,” *Phys. Rev. D*, vol. 98, December 2018.
- [44] J. Fluri, T. Kacprzak, A. Lucchi, A. Refregier, A. Amara, T. Hofmann, and A. Schneider, “Cosmological constraints with deep learning from kids-450 weak lensing maps,” *Phys. Rev. D*, vol. 100, September 2019.
- [45] D. Zuercher, J. Fluri, R. Sgier, T. Kacprzak, and A. Refregier, “Cosmological forecast for non-gaussian statistics in large-scale weak lensing surveys.” arXiv:2006.12506, June 2020.
- [46] J. Stadel, *Cosmological N-body simulations and their analysis*. PhD thesis, UNIVERSITY OF WASHINGTON, February 2001.
- [47] U. Seljak and C. Hirata, “Gravitational lensing as a contaminant of the gravity wave signal in the cmb,” *Phys. Rev. D*, vol. 69, February 2004.

- [48] A. Refregier, L. Gamper, A. Amara, and L. Heisenberg, “Pycosmo: An integrated cosmological boltzmann solver,” *Elsevier*, vol. 25, pp. 38–43, October 2018.
- [49] F. Tarsitano, U. Schmitt, A. Refregier, J. Fluri, R. Sgier, A. Nicola, J. Herbel, A. Amara, T. Kacprzak, and L. Heisenberg, “Predicting cosmological observables with pycosmo.” arXiv:2005.00543, 2020.
- [50] D. N. Limber, “The analysis of counts of the extragalactic nebulae in terms of a fluctuating density field,” *ApJ*, vol. 117, p. 134, 1953.
- [51] N. Kaiser, “Weak gravitational lensing of distant galaxies,” *ApJ*, vol. 388, pp. 272–286, April 1992.
- [52] N. Kaiser, “Weak lensing and cosmology,” *ApJ*, vol. 498, pp. 26–42, 1998.
- [53] J. A. Peacock, *Cosmological Physics*, vol. p. 704. Cambridge, UK: Cambridge University Press, January 1999.
- [54] A. Mead, J. Peacock, C. Heymans, S. Joudaki, and A. Heavens, “An accurate halo model for fitting non-linear cosmological power spectra and baryonic feedback models,” *MNRAS*, vol. 454, pp. 1958–1975, December 2015.
- [55] A. Mead, C. Heymans, L. Lombriser, J. Peacock, O. Steele, and H. Winther, “Accurate halo-model matter power spectra with dark energy, massive neutrinos and modified gravitational forces,” *MNRAS*, vol. 459, pp. 1468–1488, June 2016.
- [56] D. J. Eisenstein and W. Hu, “Baryonic features in the matter transfer function,” *ApJ*, vol. 496, pp. 605–614, March 1998.
- [57] J. Lesgourgues, “The cosmic linear anisotropy solving system (class) i: Overview.” arXiv:1104.2932, 2011.
- [58] T. Kitching, J. Alsing, A. Heavens, R. Jimenez, J. McEwen, and L. Verde, “The limits of cosmic shear,” *MNRAS*, vol. 469, pp. 2737–2749, May 2017.
- [59] S. de la Torre and L. Guzzo, “Modelling non-linear redshift-space distortions in the galaxy clustering pattern: systematic errors on the growth rate parameter,” *Mon. Not. R. Astron. Soc.*, vol. 000, pp. 1–16, 2011.
- [60] W. J. Percival, L. Samushia, A. J. Ross, C. Shapiro, and A. Raccanelli, “Redshift-space distortions,” *Phil. Trans. R. Soc. A*, vol. 369, pp. 5058–5067, 2011.
- [61] N. Padmanabhan, D. Schlegel, U. Seljak, A. Makarov, N. Bahcall, M. Blanton, J. Brinkmann, D. Eisenstein, D. Finkbeiner, J. Gunn, D. Hogg, Z. Ivezic, G. Knapp, J. Loveday, R. Lupton, R. Nichol, D. Schneider, M. Strauss, M. Tegmark, and D. York, “The clustering of luminous red galaxies in the sloandigital sky survey imaging data,” *MNRAS*, vol. 378, pp. 852–872, June 2007.
- [62] S. Dodelson, *Modern Cosmology*, vol. 0-12-219141-2. Academic Press, 2003.
- [63] R. K. Sachs and A. M. Wolfe, “Perturbations of a cosmological model and angular variations of the microwave background,” *ApJ*, vol. 147, p. 73, January 1967.
- [64] M. Rees and D. Sciamia, “Large-scale density inhomogeneities in the universe,” *Nature*, vol. 217, pp. 511–516, 1968.
- [65] N. Padmanabhan, C. Hirata, U. Seljak, D. Schlegel, J. Brinkmann, and D. Schneider, “Correlating the cmb with luminous red galaxies: The integrated sachs-wolfe effect,” *Phys. Rev. D*, vol. 72, August 2005.
- [66] E. Martinez-Gonzalez, J. L. Sanz, and J. Silk, “Anisotropies in the microwave sky due to nonlinear structures,” *ApJ*, vol. 355, pp. 5–9, May 1990.
- [67] Y.-C. Cai, S. Cole, A. Jenkins, and C. S. Frenk, “Full-sky map of the isw and rees-sciama effect from gpc simulations,” *MNRAS*, vol. 407, pp. 201–224, September 2010.

- [68] R. Crittenden and N. Turok, “Looking for a cosmological constant with the rees-sciama effect,” *Phys. Rev. Lett.*, vol. 76, p. 575, January 1996.
- [69] R. Sunyaev and Y. Zeldovich, “The velocity of clusters of galaxies relative to the microwave background. the possibility of its measurement,” *MNRAS*, vol. 190, pp. 413–420, March 1980.
- [70] D. Goldberg and D. Spergel, “Microwave background bispectrum. ii. a probe of the low redshift universe,” *Phys. Rev. D*, vol. 59, May 1999.
- [71] A. Cooray and W. Hu, “Imprint of reionization on the cosmic microwave background bispectrum,” *ApJ*, vol. 534, pp. 533–550, May 2000.
- [72] A. Lewis and A. Challinor, “Weak gravitational lensing of the cmb,” *Phys. Rep.*, vol. 429, pp. 1–65, June 2006.
- [73] C. Ma and E. Bertschinger, “Cosmological perturbation theory in the synchronous and conformal newtonian gauges,” *ApJ*, vol. 455, p. 7, December 1995.
- [74] C. Carbone, V. Springel, C. Baccigalupi, M. Bartelmann, and S. Matarrese, “Full-sky maps for gravitational lensing of the cosmic microwave background,” *MNRAS*, vol. 388, pp. 1618–1626, August 2008.
- [75] W. Hu, “Weak lensing of the cmb: A harmonic approach,” *Phys. Rev. D*, vol. 62, p. 043007, July 2000.
- [76] M. Bartelmann and P. Schneider, “Weak gravitational lensing,” *Phys. Rep.*, vol. 340, pp. 291–472, January 2001.
- [77] A. Refregier, “Weak gravitational lensing by large-scale structure,” *ARAA*, vol. 41, pp. 645–668, 2003.
- [78] C. Wallis, J. McEwen, T. Kitching, B. Leistedt, and A. Plouviez, “Mapping dark matter on the celestial sphere with weak gravitational lensing.” arXiv:1703.09233, 2017.
- [79] D. Potter, J. Stadel, and R. Teyssier, “Pkdgrav3: beyond trillion particle cosmological simulations for the next era of galaxy surveys,” *Computational Astrophysics and Cosmology*, vol. 4, May 2017.
- [80] O. Hahn and T. Abel, “Multi-scale initial conditions for cosmological simulations,” *MNRAS*, vol. 415, pp. 2101–2121, August 2011.
- [81] K. Gorski, E. Hivon, A. Banday, B. Wandelt, F. Hansen, M. Reinecke, and M. Bartelmann, “Healpix: A framework for high-resolution discretization and fast analysis of data distributed on the sphere,” *ApJ*, vol. 622, pp. 759–771, April 2005.
- [82] R. Teyssier, S. Pires, S. Prunet, D. Aubert, C. Pichon, A. Amara, K. Benabed, S. Colombi, A. Refregier, and J.-L. Starck, “Full-sky weak-lensing simulation with 70 billion particles,” *AA*, vol. 497, pp. 335–341, February 2009.
- [83] I. Smail, R. Ellis, and M. Fitchett, “Gravitational lensing of distant field galaxies by rich clusters – i. faint galaxy redshift distributions,” *MNRAS*, vol. 270, pp. 245–270, September 1994.
- [84] R. E. Smith, C. Hernandez-Monteagudo, and U. Seljak, “Impact of scale dependent bias and nonlinear structure growth on the integrated sachs-wolfe effect: Angular power spectra,” *Phys. Rev. D*, vol. 80, p. 063528, 2009.
- [85] R. Hockney and J. Eastwook, *Computer Simulations Using Particles*. CRC press, 1 ed., January 1981.
- [86] Y. Li, W. Hu, and M. Takada, “Super-sample covariance in simulations,” *Phys. Rev. D*, vol. 89, April 2014.

- [87] A. Schneider, R. Teyssier, D. Potter, J. Stadel, J. Onions, D. Reed, R. Smith, V. Springel, F. Pearce, and R. Scoccimarro, “Matter power spectrum and the challenge of percent accuracy,” *JCAP*, vol. 2016, April 2016.
- [88] M. Calabrese, C. Carbone, G. Fabbian, M. Baldi, and C. Baccigalupi, “Multiple lensing of the cosmic microwave background anisotropies,” *JCAP*, vol. 2015, March 2015.
- [89] V. Springel, M. White, and L. Hernquist, “Hydrodynamic simulations of the sunyaev-zeldovich effect(s),” *ApJ*, vol. 549, pp. 681–687, March 2001.
- [90] A. Petri, Z. Haiman, and M. May, “Validity of the born approximation for beyond gaussian weak lensing observables,” *Phys. Rev. D*, vol. 95, May 2017.
- [91] G. Pratten and A. Lewis, “Impact of post-born lensing on the cmb,” *JCAP*, vol. 2016, August 2016.
- [92] A. Barthelemy, S. Codis, and F. Bernardeau, “Post-born corrections to the one-point statistics of (cmb) lensing convergence obtained via large deviation theory,” *MNRAS*, vol. 494, pp. 3368–3382, May 2020.
- [93] S. Hagstotz, B. Schäfer, and P. Merkel, “Born-corrections to weak lensing of the cosmic microwave background temperature and polarization anisotropies,” *MNRAS*, vol. 454, pp. 831–838, November 2015.
- [94] A. Cooray and W. Hu, “Second-order corrections to weak lensing by large-scale structure,” *ApJ*, vol. 574, pp. 19–23, July 2002.
- [95] E. Krause and C. Hirata, “Weak lensing power spectra for precision cosmology. multiple-deflection, reduced shear, and lensing bias corrections,” *AA*, vol. 523, November 2010.
- [96] C. Hirata and U. Seljak, “Reconstruction of lensing from the cosmic microwave background polarization,” *Phys. Rev. D*, vol. 68, October 2003.
- [97] C. Shapiro and A. Cooray, “The born and lens-lens corrections to weak gravitational lensing angular power spectra,” *JCAP*, vol. 2006, March 2006.
- [98] S. Hilbert, J. Hartlap, S. White, and P. Schneider, “Ray-tracing through the millennium simulation: Born corrections and lens-lens coupling in cosmic shear and galaxy-galaxy lensing,” *AA*, vol. 499, pp. 31–43, May 2009.
- [99] V. Böhm, C. Modi, and E. Castorina, “Lensing corrections on galaxy-lensing cross correlations and galaxy-galaxy auto correlations,” *JCAP*, vol. 2020, March 2020.
- [100] G. Fabbian, A. Lewis, and D. Beck, “Cmb lensing reconstruction biases in cross-correlation with large-scale structure probes,” *JCAP*, vol. 2019, October 2019.
- [101] S. Hilbert, A. Barreira, G. Fabbian, P. Fosalba, C. Giocoli, S. Bose, M. Calabrese, C. Carbone, C. Davies, B. Li, C. Llinares, and P. Monaco, “The accuracy of weak lensing simulations,” *arXiv:1910.10625*.
- [102] A. J. Weiss, A. Schneider, R. Sgier, T. Kacprzak, A. Amara, and A. Refregier, “Effects of baryons on weak lensing peak statistics,” *JCAP*, vol. 2019, October 2019.
- [103] A. Schneider, R. Teyssier, J. Stadek, N. Chisari, A. L. Brun, A. Amara, and A. Refregier, “Quantifying baryon effects on the matter power spectrum and the weak lensing shear correlation,” *JCAP*, vol. 2019, March 2019.
- [104] K. Osato, M. Shirasaki, and N. Yoshida, “Impact of baryonic processes on weak lensing cosmology: Power spectrum, non-local statistics, and parameter bias,” *ApJ*, vol. 806, June 2015.
- [105] J. Wishart, “The generalised product moment distribution in samples from a normal multivariate population,” *Biometrika*, vol. 20A, pp. 32–52, December 1928.

- [106] A. Taylor, B. Joachimi, and T. Kitching, “Putting the precision in precision cosmology: How accurate should your data covariance matrix be?,” *MNRAS*, vol. 432, pp. 1928–1946, July 2013.
- [107] L. Blot, P. Corasanti, L. Amendola, and T. Kitching, “Non-linear matter power spectrum covariance matrix errors and cosmological parameter uncertainties,” *MNRAS*, vol. 458, pp. 4462–4470, March 2016.
- [108] R. C. R. N. S. B. A. M. G. R. T. Giannantonio, R. Scranton, “Combined analysis of the integrated Sachs-Wolfe effect and cosmological implications,” *Phys. Rev. D*, vol. 77, June 2008.
- [109] D. B. J. B. G. B. E. B. S. B. M. B. D. C. e. a. C. Heymans, L. Van Waerbeke, “The shear testing programme – i. weak lensing analysis of simulated ground-based observations,” *MNRAS*, vol. 368, pp. 1323–1339, May 2006.
- [110] B. Wandelt, E. Hivon, and K. Gorski, “Cosmic microwave background anisotropy power spectrum statistics for high precision cosmology,” *Phys. Rev. D*, vol. 64, September 2001.
- [111] E. Hivon, K. Gorski, C. Netterfield, B. Crill, S. Prunet, and F. Hansen, “Master of the cosmic microwave background anisotropy power spectrum: A fast method for statistical analysis of large and complex cosmic microwave background data sets,” *ApJ*, vol. 567, no. 1, 2002.
- [112] P. Peebles, “Statistical analysis of catalogs of extragalactic objects. i. theory,” *ApJ*, vol. 185, pp. 413–440, October 1973.
- [113] E. Sellentin and A. Heavens, “Parameter inference with estimated covariance matrices,” *MNRAS*, vol. 456, pp. 132–136, February 2016.
- [114] E. Sellentin and A. Heavens, “Quantifying lost information due to covariance matrix estimation in parameter inference,” *MNRAS*, vol. 464, pp. 4658–4665, February 2017.
- [115] D. L. J. G. D. Foreman-Mackey, D.W. Hogg, “emcee: The mcmc hammer,” *PASP*, vol. 125, pp. 306–312, March 2013.
- [116] D. Smoot, C. Bennett, and A. K. et al., “Structure in the COBE differential microwave radiometer first-year maps,” *ApJ*, vol. 396, September 1992.
- [117] G. Efstathiou, “Myths and truths concerning estimation of power spectra: the case for a hybrid estimator,” *MNRAS*, vol. 349, pp. 603–626, April 2004.
- [118] M. Brown, P. Castro, and A. Taylor, “CMB temperature and polarisation pseudo-cl estimators and covariances,” *MNRAS*, vol. 360, pp. 1262–1280, July 2005.
- [119] A. Kogut, D. Spergel, C. Barnes, C. Bennett, M. Halpern, G. Hinshaw, N. Jarosik, M. Limon, S. Meyer, and L. Page, “Wilkinson microwave anisotropy probe (WMAP) first year observations: The polarization,” *ApJ*, vol. 128, pp. 161–173, September 2003.
- [120] M. Rotenberg, R. Bivins, N. Metropolis, and J. Wooten, *The 3-j and 6-j symbols*. The Technology Press, MIT, 1959.
- [121] A. Lewis, “Lensed CMB simulation and parameter estimation,” *Phys. Rev. D*, vol. 71, April 2005.
- [122] A. Challinor and A. Lewis, “Lensed CMB power spectra from all-sky correlation functions,” *Phys. Rev. D*, vol. 71, May 2005.
- [123] C. Carbone, C. Baccigalupi, M. Bartelmann, S. Matarrese, and V. Springel, “Lensed CMB temperature and polarization maps from the millennium simulation,” *MNRAS*, vol. 396, pp. 668–679, June 2009.

A Analytical Prediction for the ISW Auto-Correlation

This detailed derivation of the auto-correlation of the CMB temperature anisotropies due to the ISW effect follows closely Appendix F in Nicola *et al.* [11], where the analytical prediction

for the cross-correlation between the CMB temperature anisotropies and weak lensing shear is derived. The ISW effect leads to the generation of CMB temperature anisotropies given by equation (2.7), which can be decomposed into spherical harmonics with multipole coefficients

$$\Delta T_{\text{ISW},\ell m} = 4\pi i^\ell 2 T_{\text{CMB}} \int_{\eta_r}^{\eta_0} d\eta \int \frac{d\vec{k}}{(2\pi)^3} \frac{d}{d\eta} \Phi(\vec{k}, z) j_\ell(k\chi(z)) Y^*(\hat{n}_k). \quad (\text{A.1})$$

The spherical harmonic power spectrum for the CMB temperature anisotropies due to the ISW effect is defined as

$$\langle \Delta T_{\text{ISW},\ell m} \Delta T_{\text{ISW},\ell' m'} \rangle = C_\ell^{\text{ISW}} \delta_{\ell\ell'} \delta_{mm'}, \quad (\text{A.2})$$

and can be written as

$$C_\ell^{\text{ISW}} = (4\pi)^2 4 T_{\text{CMB}}^2 \left\langle \int_0^{z_*} dz \int \frac{k^2 dk}{(2\pi)^3} \frac{d}{dz} [D(z)(1+z)] \Phi(\vec{k}, z=0) j_\ell(k\chi(z)) \right. \\ \left. \times \int_0^{z_*} dz' \int \frac{k'^2 dk'}{(2\pi)^3} \frac{d}{dz'} [D(z')(1+z')] \Phi(\vec{k}', z'=0) j_\ell(k'\chi(z')) \right\rangle, \quad (\text{A.3})$$

where we used equation (A.1) and the fact that in linear perturbation theory one can separate the time- and scale-dependence of the gravitational potential $\Phi(k, z) = \Phi(k, z=0)D(z)(1+z)$. The linear power spectrum of the gravitational potential at present time is defined as

$$\langle \Phi(\vec{k}, z=0) \Phi(\vec{k}', z'=0) \rangle = (2\pi)^3 P_{\Phi\Phi}^{\text{lin}}(k, z=0) \delta^{\text{D}}(\vec{k} - \vec{k}'), \quad (\text{A.4})$$

and is related to the matter power spectrum through Poisson's equation as

$$P_{\Phi\Phi}^{\text{lin}}(k, z=0) = \left(\frac{3}{2}\right)^2 \frac{\Omega_m^2 H_0^4}{c^4} \frac{P_{\delta\delta}^{\text{lin}}(k, z=0)}{k^4}, \quad (\text{A.5})$$

where $\delta^{\text{D}}(\vec{k} - \vec{k}')$ denotes the Dirac delta function. The expression for the spherical harmonic power spectrum given by equation (A.3) can be further simplified using equations (A.4) and (A.5) to

$$C_\ell^{\text{ISW}} = (4\pi)^2 T_{\text{CMB}}^2 \left(\frac{3\Omega_m H_0^2}{c^2}\right)^2 \int_0^{z_*} dz \int \frac{k^2 dk}{(2\pi)^3} \frac{d}{dz} [D(z)(1+z)] \\ \times \int_0^{z_*} dz' \frac{d}{dz'} [D(z')(1+z')] \frac{P_{\delta\delta}^{\text{lin}}(k, z=0)}{k^4} j_\ell(k\chi(z)) j_\ell(k\chi(z')). \quad (\text{A.6})$$

We further use the Limber approximation ([50], [51], [52]) to simplify the calculation of equation (A.6) giving

$$C_\ell^{\text{ISW}} = T_{\text{CMB}}^2 \left(\frac{3\Omega_m H_0^2}{c^2}\right)^2 \frac{1}{(\ell + 1/2)^4} \int dz \frac{d}{dz} [D(z)(1+z)]^2 \chi(z)^2 \\ \times P_{\delta\delta}^{\text{lin}}\left(k = \frac{\ell + 1/2}{\chi(z)}, 0\right). \quad (\text{A.7})$$

B Shot Noise Estimation

In this section we will derive a estimation for the shot noise contribution to the convergence spherical harmonic power spectrum $C_\ell^{\text{sn}, \text{Born}}$ based on the Born approximation. The shot noise of each shell is inverse proportional to the mean particle density of the sphere, which can be calculated analytically. This calculation assumes that the shot noise of different shells are uncorrelated and that the signal and the shot noise are also uncorrelated. With this assumption, we can write the overdensity on a spherical shell as

$$\delta = \frac{\rho - \bar{\rho}}{\bar{\rho}}, \quad (\text{B.1})$$

where the density ρ describes a Poisson point process on that shell and is proportional to the number of particles in the simulation N_p . The Poisson shot noise contribution to the spherical harmonic power spectrum is then given by

$$C_\ell^{\text{shotnoise}} = \frac{4\pi}{N_p}. \quad (\text{B.2})$$

Our pipeline UFALCON computes the convergence from N -Body simulation outputs using the Born approximation as

$$\kappa(\text{pix}) \approx \frac{3}{2} \Omega_m \sum_b W_b \frac{H_0}{c} \left[\frac{N_{\text{pix}}}{4\pi} \frac{V_{\text{sim}}}{N_p^{\text{sim}}} \left(\frac{H_0}{c} \right)^2 \frac{n_p}{\mathcal{D}^2(z_b)} \right], \quad (\text{B.3})$$

where $n_p = n_p(\text{pix}, \Delta z_b)$ is the number of particles per pixel in the shell $\Delta z_b = z_b^{\text{max}} - z_b^{\text{min}}$. The comoving volume of shell b (in Mpc) can be written as

$$V_b = \frac{4}{3} \pi \left(\frac{c}{H_0} \right)^3 [\mathcal{D}^3(z_b^{\text{max}}) - \mathcal{D}^3(z_b^{\text{min}})]. \quad (\text{B.4})$$

The mean density of a shell (per pixel) is then given by

$$\bar{n}_p = \rho \cdot \frac{V_b}{N_{\text{pix}}} = \left(\frac{N_p^{\text{sim}}}{V_{\text{sim}}} \right) \frac{V_b}{N_{\text{pix}}}. \quad (\text{B.5})$$

The terms in the expression for the convergence can then be rearranged in order to obtain the shot noise contribution of each individual shell

$$\begin{aligned} \kappa(\text{pix}) &\approx \frac{3}{2} \Omega_m \sum_b W_b \frac{H_0}{c} \left[\frac{N_{\text{pix}}}{4\pi} \frac{V_{\text{sim}}}{N_p^{\text{sim}}} \left(\frac{H_0}{c} \right)^2 \frac{\bar{n}_p}{\mathcal{D}^2(z_b)} \frac{n_p}{\bar{n}_p} \right] \\ &= \frac{3}{2} \Omega_m \sum_b W_b \left(\frac{H_0}{c} \right)^3 \frac{1}{4\pi} \frac{V_b}{\mathcal{D}^2(z_b)} \left[\frac{n_p}{\bar{n}_p} \right]. \end{aligned} \quad (\text{B.6})$$

The shot noise contribution to the spherical harmonic power spectrum of the convergence using the Born approximation is therefore given by

$$C_\ell^{\text{sn}, \text{Born}} = \left[\frac{3}{2} \Omega_m \left(\frac{H_0}{c} \right)^3 \frac{1}{4\pi} \right]^2 \sum_b \left[W_b \frac{V_b}{\mathcal{D}^2(z_b)} \right]^2 \frac{4\pi}{N_b}, \quad (\text{B.7})$$

where N_b is the number of particles in the shell b and can be expressed as

$$N_b = \frac{N_p^{\text{sim}}}{V_{\text{sim}}} V_b. \quad (\text{B.8})$$

In Figure 16 we show the comparison of the shot noise contribution to the weak lensing convergence power spectrum based on the Limber (equation (3.15) in section 3.3.3) and Born (equation B.7) approximations.

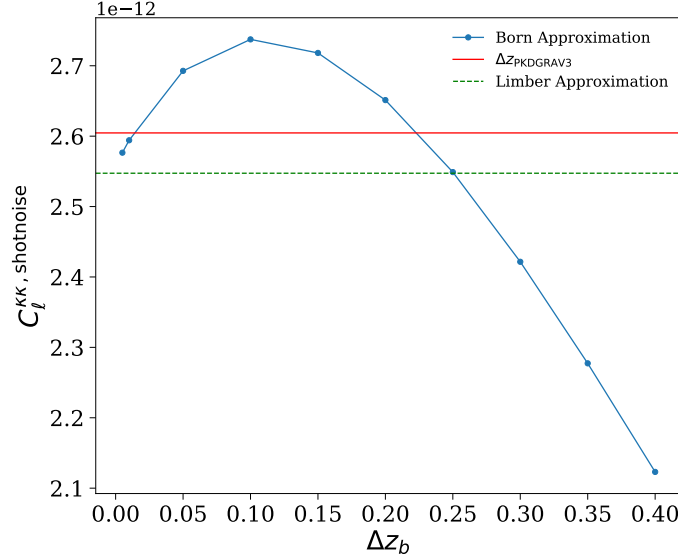


Figure 16: The shot noise based on the Born approximation is given by the blue line and depends on the choice of shell thickness Δz_b , which generally increases when choosing thinner shells. The drop in power for shells smaller than ~ 0.1 is explained by the $1/\mathcal{D}^2(z_b)$ factor in equation (3.16). The horizontal red solid line represents the shot noise obtained when using the non-constant redshift-spacing from our PKDGRAV3 simulation run. The shot noise based on the Limber approximation is given by the horizontal green dashed line and is independent of shell-thickness.

C Correlated Gaussian Maps

Here we describe our routine used in section 5 to generate sets of correlated Gaussian spin-0 maps from prescribed auto- and cross-power spectra, which can be used to estimate the power spectrum covariance matrix.

Our implementation is based on the general algorithm presented in Giannantonio *et al.* [108] and implemented and extended to spin-2 field in Nicola *et al.* [11, 12]. This algorithm is based on the HEALPIX subroutine **synfast**, which is used to generate maps from an input spherical harmonic power spectrum C_{ℓ}^{ii} and probe i . Thereby a random phase ξ with mean zero $\langle \xi \rangle = 0$ and unit variance $\langle \xi \xi^* \rangle = 1$ is assigned to each spherical harmonic mode ℓ . The correct power spectrum is then ensured by setting

$$a_{\ell m}^i = \sqrt{C_{\ell}^{ii}} \xi, \quad (\text{C.1})$$

which is effectively implemented in **synfast**. In the general case, we consider n maps and therefore require n different phases, which are assumed uncorrelated $\langle \xi_i \xi_j^* \rangle = \delta_{ij}$. The spherical harmonics are then given by

$$a_{\ell m}^1 = \xi_1 T_{11} \quad (\text{C.2})$$

$$a_{\ell m}^2 = \xi_1 T_{21} + \xi_2 T_{22} \quad (\text{C.3})$$

$$a_{\ell m}^3 = \xi_1 T_{31} + \xi_2 T_{32} + \xi_3 T_{33} \quad (\text{C.4})$$

$$\dots, \quad (\text{C.5})$$

which satisfy the constraints $\langle a_{\ell m}^i a_{\ell' m'}^{j*} \rangle = C_{\ell}^{ij} \delta_{\ell\ell'} \delta_{mm'}$. This gives $n(n+1)/2$ equations for the unknown amplitudes T_{ij} given by

$$C_{\ell}^{11} = T_{11}^2 \quad (\text{C.6})$$

$$C_{\ell}^{12} = T_{11} T_{21} \quad (\text{C.7})$$

$$C_{\ell}^{22} = T_{21}^2 + T_{22}^2 \quad (\text{C.8})$$

$$C_{\ell}^{13} = T_{11} T_{31} \quad (\text{C.9})$$

$$\dots. \quad (\text{C.10})$$

The general recursive relation for the amplitudes is given by [108]

$$T_{ij} = \sqrt{C_{\ell m}^{ji} - \sum_{k=1}^{j-1} T_{ik}^2} \quad , \quad \text{if } i = j \quad (\text{C.11})$$

$$T_{ij} = \frac{C_{\ell m}^{ji} - \sum_{k=1}^{j-1} T_{ik} T_{jk}}{T_{jj}} \quad , \quad \text{if } i > j. \quad (\text{C.12})$$

In practice, we have implemented this relation using **synfast** with $n = 4$ different *random seeds*, corresponding to the different phases ξ , to generate correlated Gaussian maps for the probes ΔT_{ISW} , κ_{CMB} , δ_g and κ_{small} .

D Pseudo- C_{ℓ} Estimation

It is well known that limited coverage of the celestial sphere poses a real challenge for the measurement of the auto- and cross-power spectra. Since the discovery of the CMB radiation anisotropy by the *COBE* satellite (Smoot *et al.* [116]), numerous power spectrum estimators for the analysis of large CMB temperature data sets have been developed (an overview is given in [117]).

Our implementation of the pseudo- C_{ℓ} method is based on [118] and [119], which applies to temperature- and polarisation-type fields denoted by T and P . The effect of finite window functions is then given by [118]

$$\tilde{T}(\hat{n}) = W_T(\hat{n}) T(\hat{n}) \quad , \quad \tilde{P}(\hat{n}) = W_P(\hat{n}) P(\hat{n}) \quad , \quad (\text{D.1})$$

where $W_T(\hat{n})$ and $W_P(\hat{n})$ denote the window functions for the two field types pointing in direction \hat{n} on the sky and are in general not equal. Note that the window functions vanish outside of the survey area. Within the survey, the window function can also take into account weighting of the field, which depends on the specific survey considered. The observed cut-sky

power spectra are related to the underlying full-sky analytical predictions based on PyCosmo by the matrix relation

$$\tilde{\mathbf{C}}_\ell = \sum_{\ell'} \mathbf{M}_{\ell\ell'} \mathbf{C}_{\ell'}^{\text{PyCosmo}}, \quad (\text{D.2})$$

where \mathbf{M} is the mode-coupling matrix describing the effect of the mask applied to the data. This relation can be expanded as

$$\begin{pmatrix} \tilde{C}_\ell^{TT} \\ \tilde{C}_\ell^{TE} \\ \tilde{C}_\ell^{TB} \\ \tilde{C}_\ell^{EE} \\ \tilde{C}_\ell^{EB} \\ \tilde{C}_\ell^{BB} \end{pmatrix} = \sum_{\ell'} \begin{pmatrix} M_{\ell\ell'}^{TT,TT} & 0 & 0 & 0 & 0 & 0 \\ 0 & M_{\ell\ell'}^{TE,TE} & M_{\ell\ell'}^{TE,TB} & 0 & 0 & 0 \\ 0 & M_{\ell\ell'}^{TB,TE} & M_{\ell\ell'}^{TB,TB} & 0 & 0 & 0 \\ 0 & 0 & 0 & M_{\ell\ell'}^{EE,EE} & M_{\ell\ell'}^{EE,EB} & M_{\ell\ell'}^{EE,BB} \\ 0 & 0 & 0 & M_{\ell\ell'}^{EB,EE} & M_{\ell\ell'}^{EB,EB} & M_{\ell\ell'}^{EB,BB} \\ 0 & 0 & 0 & M_{\ell\ell'}^{BB,EE} & M_{\ell\ell'}^{BB,EB} & M_{\ell\ell'}^{BB,BB} \end{pmatrix} \begin{pmatrix} C_{\ell'}^{TT} \\ C_{\ell'}^{TE} \\ C_{\ell'}^{TB} \\ C_{\ell'}^{EE} \\ C_{\ell'}^{EB} \\ C_{\ell'}^{BB} \end{pmatrix}, \quad (\text{D.3})$$

where the temperature T and the E and B modes represent any spin-0 and spin-2 fields respectively. The coupling terms can be simplified using the symmetry and orthogonality properties of the Wigner-3j symbols [120]. Our implementation of the non-zero mode-coupling terms is based on equations (A12) - (A17) in [118], and is given by the following set of expressions:

$$\begin{aligned} M_{\ell\ell'}^{TT,TT} &= \frac{(2\ell'+1)}{4\pi} \sum_{\ell''} (2\ell''+1) \mathcal{W}_{\ell''}^{TT} \begin{pmatrix} \ell & \ell' & \ell'' \\ 0 & 0 & 0 \end{pmatrix}^2 \\ M_{\ell\ell'}^{TE,TE} &= M_{\ell\ell'}^{TB,TB} = \frac{(2\ell'+1)}{4\pi} \sum_{\ell''} (2\ell''+1) \mathcal{W}_{\ell''}^{TP} \begin{pmatrix} \ell & \ell' & \ell'' \\ 0 & 0 & 0 \end{pmatrix} \begin{pmatrix} \ell & \ell' & \ell'' \\ 2 & -2 & 0 \end{pmatrix} \\ M_{\ell\ell'}^{EE,EE} &= M_{\ell\ell'}^{BB,BB} = \frac{(2\ell'+1)}{8\pi} \sum_{\ell''} (2\ell''+1) \mathcal{W}_{\ell''}^{PP} \left[1 + (-1)^{\ell+\ell'+\ell''} \right] \begin{pmatrix} \ell & \ell' & \ell'' \\ 2 & -2 & 0 \end{pmatrix}^2 \\ M_{\ell\ell'}^{EE,BB} &= M_{\ell\ell'}^{BB,EE} = \frac{(2\ell'+1)}{8\pi} \sum_{\ell''} (2\ell''+1) \mathcal{W}_{\ell''}^{PP} \left[1 - (-1)^{\ell+\ell'+\ell''} \right] \begin{pmatrix} \ell & \ell' & \ell'' \\ 2 & -2 & 0 \end{pmatrix}^2 \\ M_{\ell\ell'}^{EB,EB} &= \frac{(2\ell'+1)}{4\pi} \sum_{\ell''} (2\ell''+1) \mathcal{W}_{\ell''}^{PP} \begin{pmatrix} \ell & \ell' & \ell'' \\ 2 & -2 & 0 \end{pmatrix}^2. \end{aligned} \quad (\text{D.4})$$

The kernels in equation (D.4) depend on the geometry of the cut sky and are expressed in terms of the auto- and cross-power spectra of the window functions $W_T(\hat{n})$ and $W_P(\hat{n})$, which are given by

$$\begin{aligned} \mathcal{W}_\ell^{TT} &= \frac{1}{2\ell+1} \sum_m w_{\ell m}^T (w_{\ell m}^T)^*, \\ \mathcal{W}_\ell^{PP} &= \frac{1}{2\ell+1} \sum_m w_{\ell m}^P (w_{\ell m}^P)^*, \\ \mathcal{W}_\ell^{TP} &= \frac{1}{2\ell+1} \sum_m w_{\ell m}^T (w_{\ell m}^P)^*, \end{aligned} \quad (\text{D.5})$$

where $w_{\ell m}^T$ and $w_{\ell m}^P$ are the spherical harmonic coefficients of the window functions

$$w_{\ell m}^T = \int d\hat{n} W_T(\hat{n}) Y_{\ell m}^* \quad , \quad w_{\ell m}^P = \int d\hat{n} W_P(\hat{n}) Y_{\ell m}^*. \quad (\text{D.6})$$

Note that for the term $M_{\ell\ell'}^{EE,BB}$ we have adopted the correct sign given by (A17) in [119], which differs from the sign used in equation (A15) in [118]. Furthermore, we have explicitly written out the prefactors $(2\ell'' + 1)$ in the coupling terms (analogous to equation (A31) in [111]). We numerically compute the Wigner-3j symbols using the PYSHTOOLS¹⁸ package.

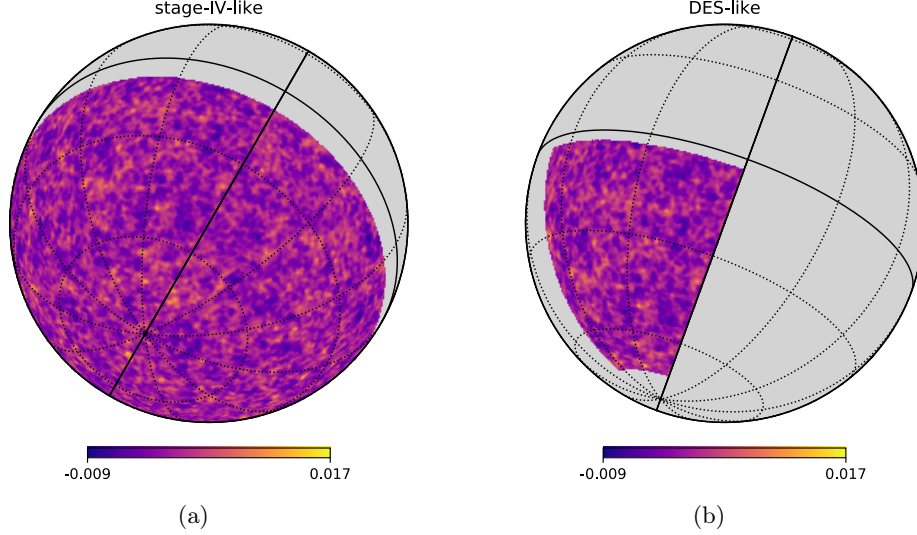


Figure 17: Weak lensing mass maps for different sky cuts. Left: stage IV-like geometry as used in this work. Right: DES Y3-like survey footprint.

For testing purposes, we applied our pseudo- C_ℓ method on the weak lensing convergence (denoted by T) and shear (denoted by E and B) spherical harmonic power spectra. Hereby we used a stage-IV-like and DES Y3-like survey geometry, as shown in Figure 17. We first computed analytical predictions for the power spectra using PYCOSMO, denoted by true- C_ℓ . To obtain a reference for the effect of the sky cut, we generated Gaussian maps from the true- C_ℓ 's using `synfast`, applied the masks on a map level and computed the masked power spectra using `anafast`. In Figure 18, we show the ratios between the masked power spectra described above and the pseudo- C_ℓ based on our method and when simply multiplying the true- C_ℓ 's with f_{sky} . Note that we only consider one synthetic Gaussian realization for the masked power spectrum. We observe that our results for the pseudo- C_ℓ 's closely follow the masked power spectra. The results using the true- $C_\ell \times f_{\text{sky}}$ are significantly lacking power at higher multipoles, starting at $\ell \sim 500$. A simple multiplication with f_{sky} only corrects the true- C_ℓ 's for the covered fraction of the sky, but does not take into account the coupling between the different modes, which is especially important when applying complicated sky cuts.

¹⁸<https://pypi.org/project/pyshtools/>

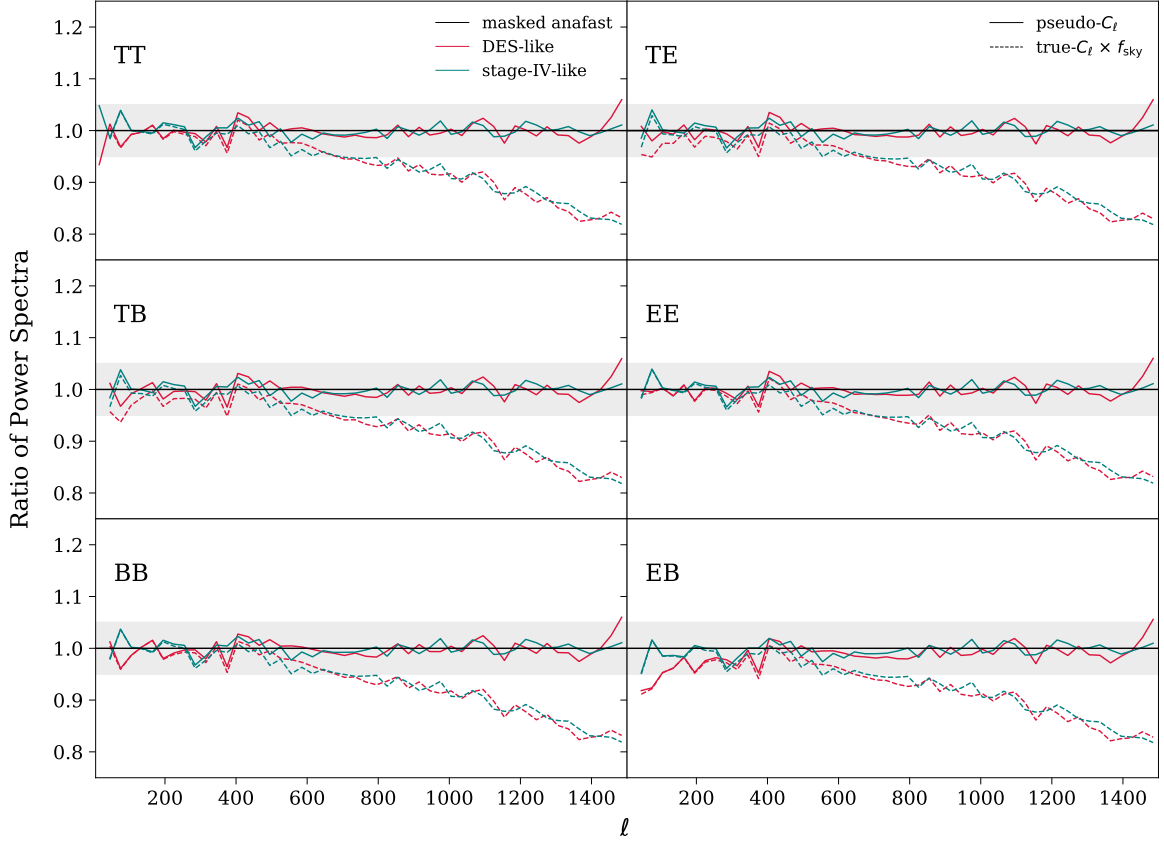


Figure 18: Ratio between one realization of the masked power spectra (obtained by applying the mask on a map level) and the pseudo- C_ℓ (using equation (D.2) on the true- C_ℓ ; solid lines) and by multiplying the true- C_ℓ with f_{sky} (dashed lines). The different panels show the ratios of the weak lensing convergence (T) and shear (E and B) auto- and cross-spherical harmonic power spectra for a stage IV-like (dark cyan) and a DES Y3-like (red) mask. The grey band denotes 5% deviation from the masked power spectra.

E CMB Lensing

The weak gravitational lensing of the CMB represents one of the most important mechanisms which can generate secondary anisotropies and induce non-Gaussian features in the observed CMB sky [72]. In this section we show the capability of our CMB lensing potential maps, generated using UFALCON, to perform weak gravitational lensing of the different CMB fields without emphasis on quantitative results.

The temperature and polarisation fields are moved from a initial angular position $\vec{\theta}$ to a new position $\vec{\theta} + \vec{\alpha}$, where $\vec{\alpha} = \nabla_{\hat{n}}\psi$ represents the deflection angle and $\nabla_{\hat{n}}$ is the two-dimensional transverse derivative w.r.t. the line-of-sight pointing in direction $\hat{n} \equiv (\theta, \phi)$ on the sky. This requires accurate interpolation on the pixels (lensed rays are not at centers of pixels), which is why we used the LENSPIX¹⁹ package [121], [122]. The original code uses a Gaussian realization of the lensing potential power spectrum obtained using the publicly

¹⁹<https://cosmologist.info/lenspix/>

available Code for Anisotropies in the Microwave Background (CAMB²⁰). We modified the `HealpixInterpLensedMapGradPhi` subroutine in the code in order to read the deflection angle we obtained from our simulation, capturing the non-linear and non-Gaussian features. This approach has previously been applied in [123] and [27]. In Figure 3 (in the main text) we show the deflection angle modulus $|\vec{\alpha}| = \sqrt{(\Delta\theta)^2 + (\Delta\phi)^2}$ we obtained by directly performing the angular derivative on our lensing potential map with $n_{\text{side}}=1024$. In Figure 19 we show all the spherical harmonic power spectra binned with $\delta\ell = 10$ obtained when using LENSPIX with our simulation-based deflection angle as input. Our results are compared to the lensed and unlensed CMB power spectra based on the full-sky correlation function technique implemented in CAMB [122]. Note that we have used $\ell_{\text{max}} = 1500$ in LENSPIX and chosen our fiducial cosmological parameters given by equation (3.1).

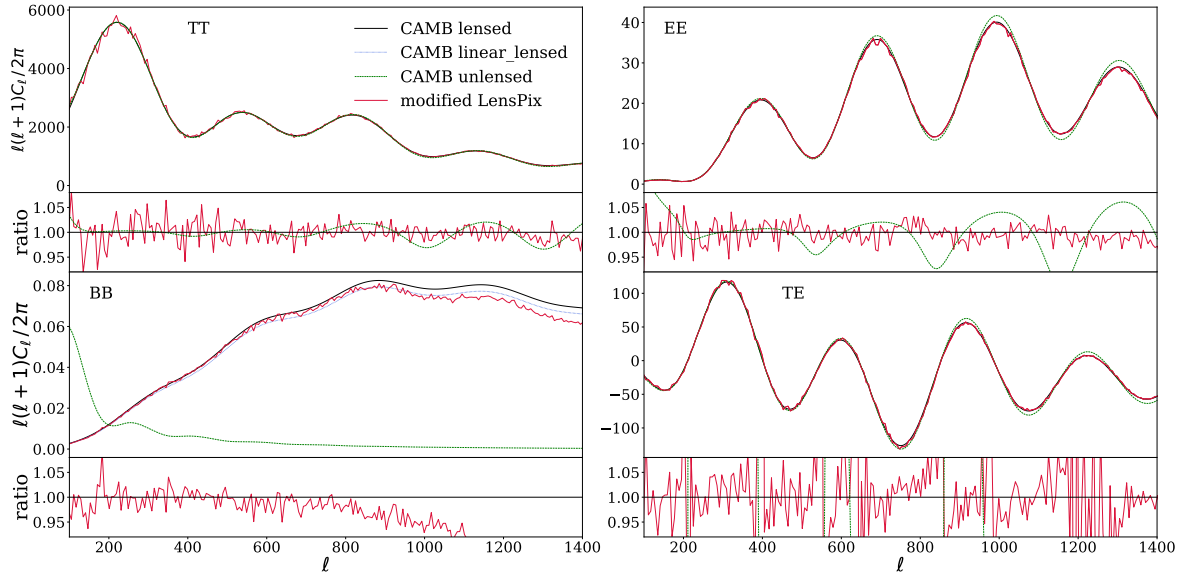


Figure 19: Simulated lensed TT -, EE -, TE - and BB -spherical harmonic power spectra (in μK^2) (solid red lines) generated using the modified-LENSPIX code with our UFALCON-based deflection angle. Our results are compared to the nonlinearly and linearly lensed and unlensed CAMB predictions (solid black, dotted blue and dashed green lines respectively). Our simulation results correspond to one realization and is binned with $\delta\ell = 10$.

Our modified-LENSPIX results for the TT -, EE - and TE - power spectra agree within 5% with the nonlinearly lensed CAMB predictions up to $\ell \sim 1500$, where CMB lensing has led to a transfer of power from larger to smaller scales, smearing out the acoustic peaks. For these cases we do not show the linearly lensed CAMB power spectra, since we expect the nonlinear effects to become important at $\ell < 2500$ [123]. In the BB -case, the nonlinearities present in the lensing potential are affecting all scales of the lens-induced B -mode power spectrum. This effect is expected to be already of the order of $\sim 7.5\%$ for multipoles $\ell \leq 10^3$ [123]. Our modified-LENSPIX B -mode results agree to the nonlinearly lensed CAMB prediction up to $\ell \sim 500$ and to the linearly lensed CAMB prediction up to $\ell \sim 10^3$. This result clearly indicates the missing lensing signal in our simulation-based lensing potential, which covers the range from $z = 0$ to 1.75. Even though the most relevant redshift for CMB lensing is at

²⁰<http://camb.info/>

about $z \sim 1$, we therefore expect to neglect a significant amount of the lensing power. We leave a more detailed treatment of CMB lensing by extending the integration range in our pipeline to future work.

F Parameter Constraints with Nuisance Parameters

In this section we show the parameter contours discussed in 5 including the 4 nuisance parameters $\{m_T, m_\delta, m_\gamma, m_\kappa\}$, with $T = \Delta T_{\text{ISW}}$, $\delta = \delta_g$, $\kappa = \kappa_{\text{CMB}}$ and $\gamma = \gamma_1$ for notational brevity. We assume flat priors for all the nuisance parameters $m_i \in [-0.2, 0.2]$.

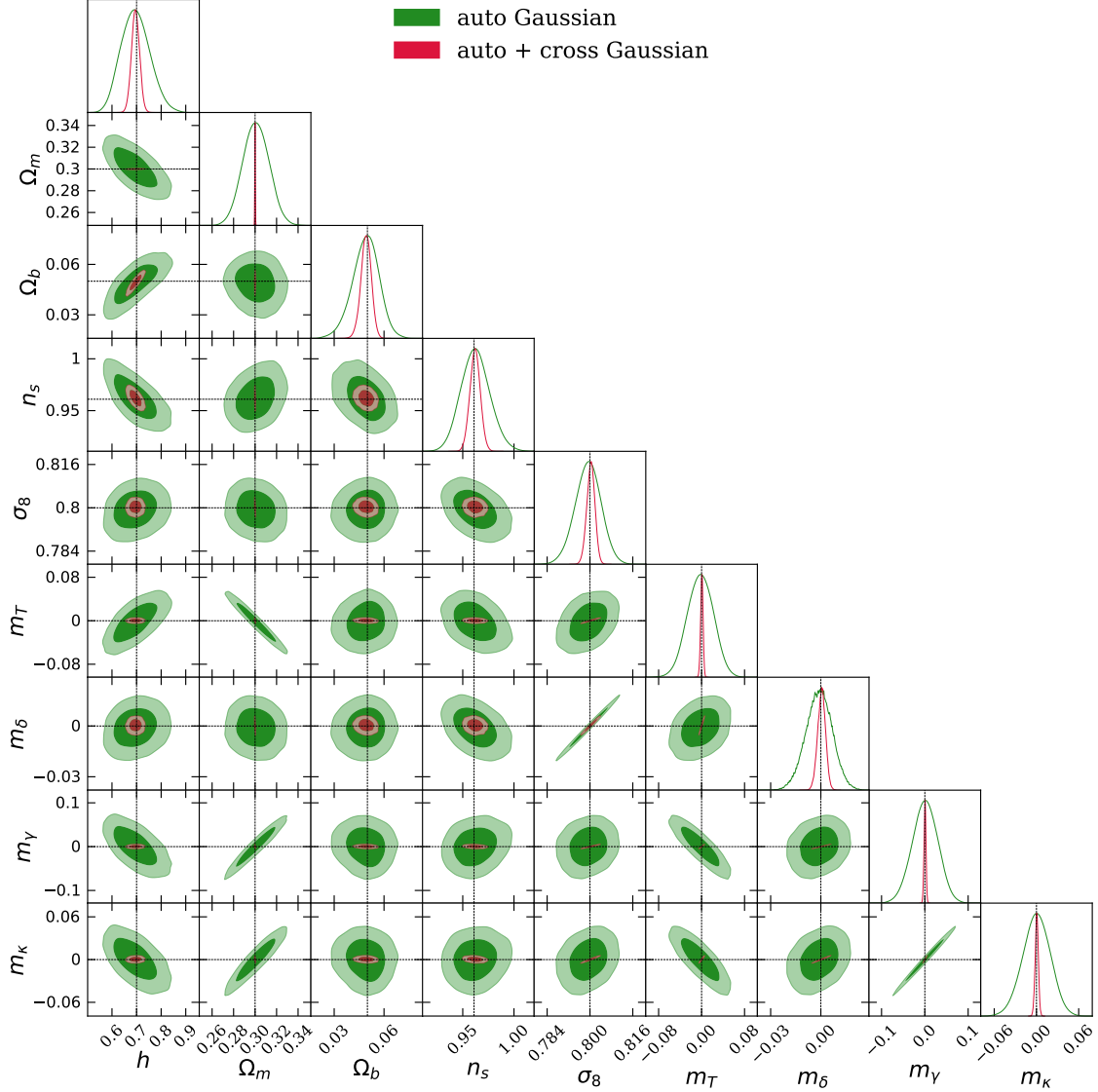


Figure 20: Parameter constraints for the parameters described in section 5 including the 4 nuisance parameters $\{m_T, m_\delta, m_\gamma, m_\kappa\}$. The triangle-plot show the contours obtained when using a Gaussian covariance matrix. The green and red contours are obtained using only the auto-power spectra and the auto- and cross-power spectra respectively. The inner (outer) contours depict the 68% (95%) confidence levels.

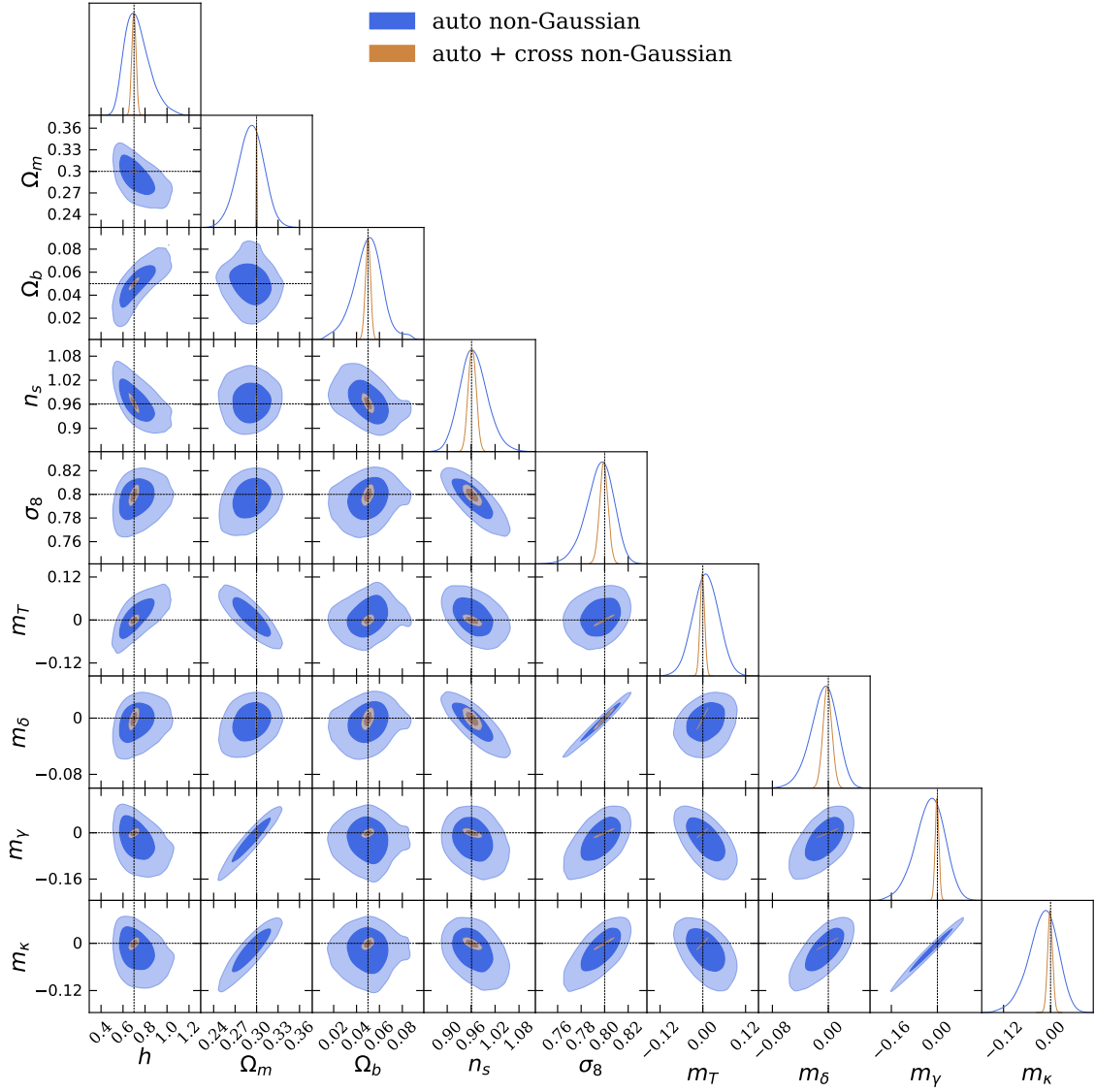


Figure 21: Parameter constraints for the parameters described in section 5 including the 4 nuisance parameters $\{m_T, m_\delta, m_\gamma, m_\kappa\}$. The triangle-plot show the contours obtained when using a simulation-based non-Gaussian covariance matrix. The blue and brown contours are obtained using only the auto-power spectra and the auto- and cross-power spectra respectively. The inner (outer) contours depict the 68% (95%) confidence levels.

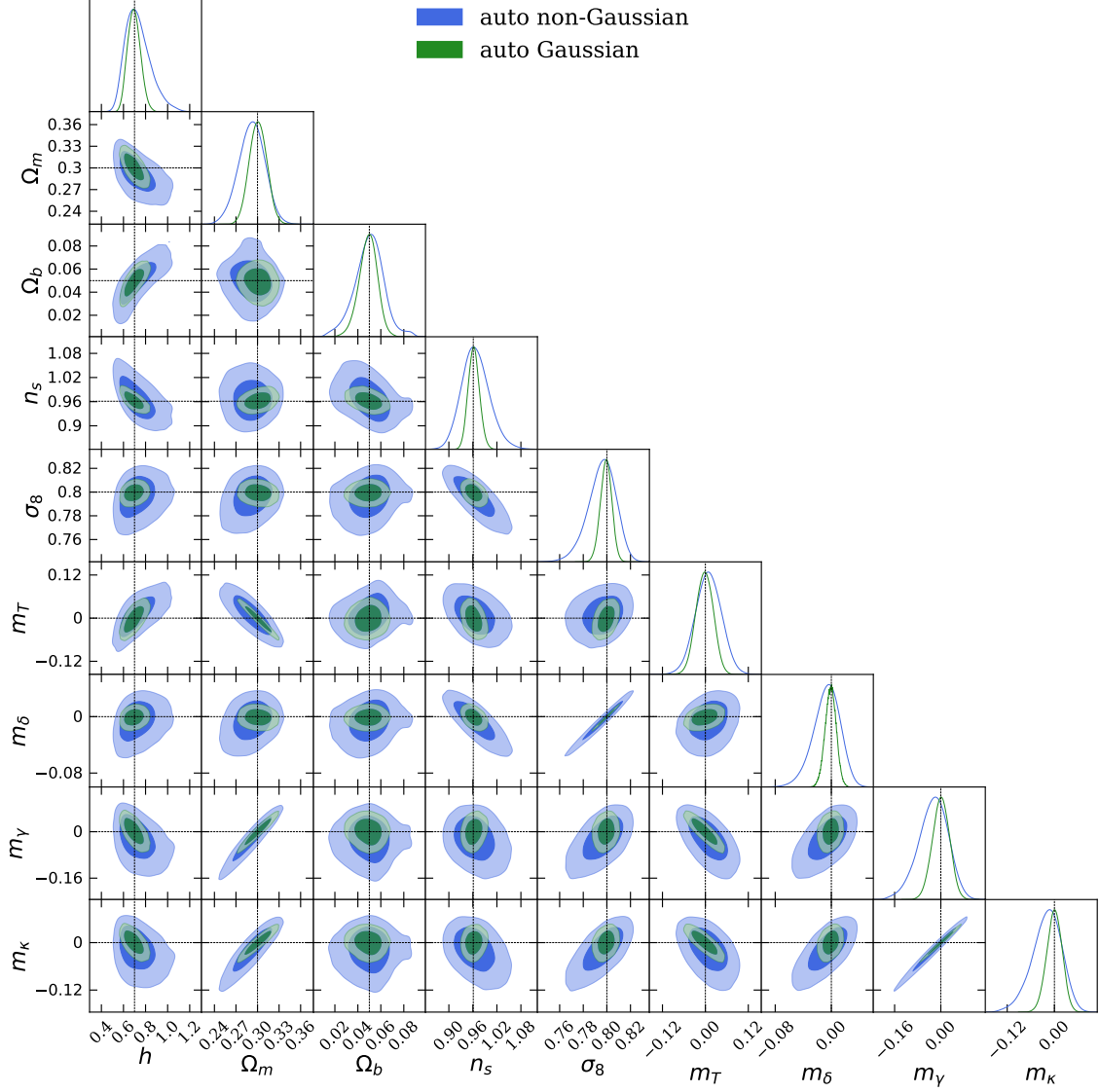


Figure 22: Parameter constraints for the parameters described in section 5 including the 4 nuisance parameters $\{m_T, m_\delta, m_\gamma, m_\kappa\}$. The triangle-plot show the contours obtained when using the auto-power spectra only. The blue (green) contours are obtained by using a non-Gaussian (Gaussian) covariance matrix. The inner (outer) contours depict the 68% (95%) confidence levels.

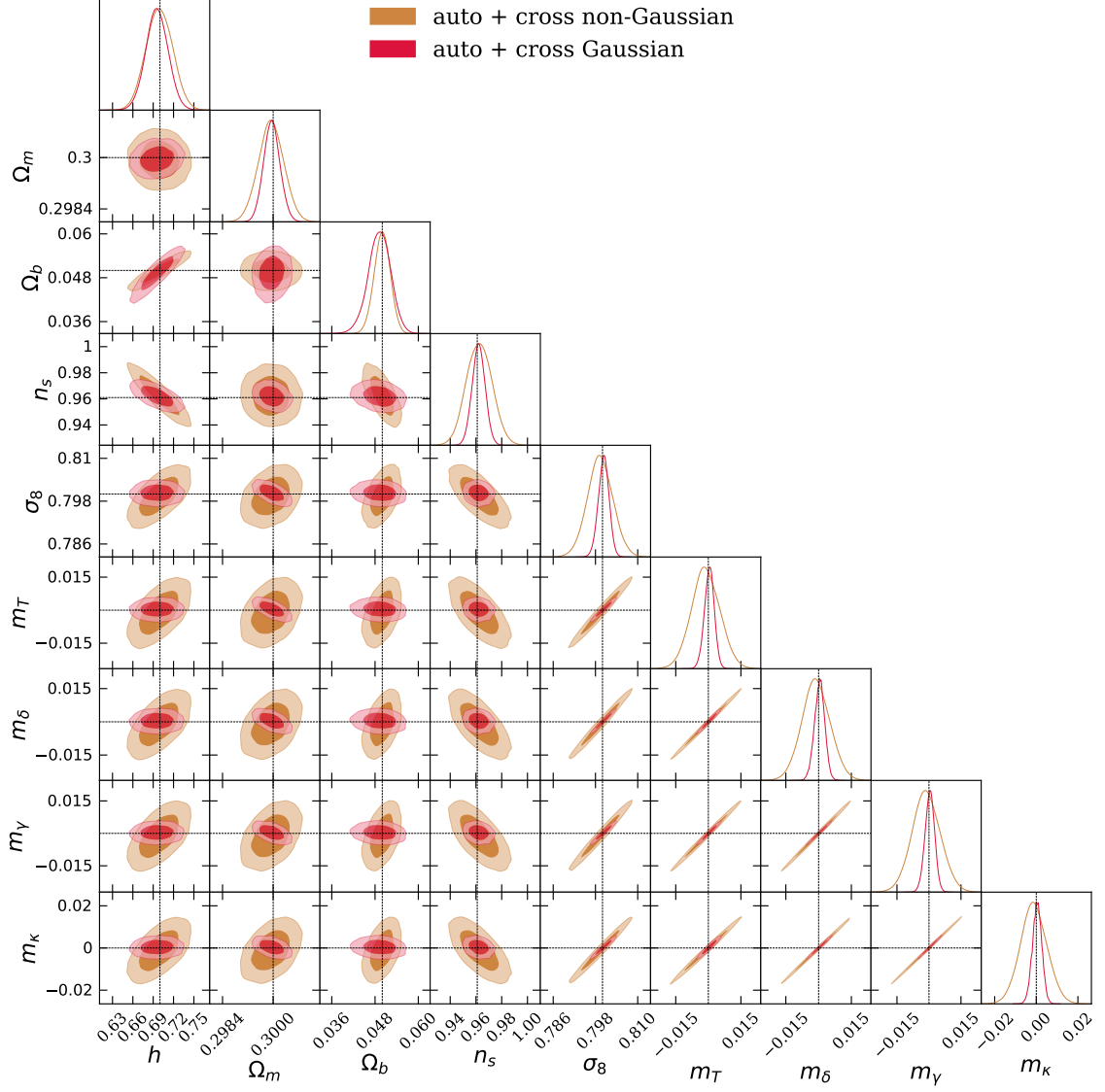


Figure 23: Parameter constraints for the parameters described in section 5 including the 4 nuisance parameters $\{m_T, m_\delta, m_\gamma, m_\kappa\}$. The triangle-plot show the contours obtained when using the auto- and cross-power spectra. The brown (red) contours are obtained by using a non-Gaussian (Gaussian) covariance matrix. The inner (outer) contours depict the 68% (95%) confidence levels.